
This is an electronic reprint of the original article.
This reprint may differ from the original in pagination and typographic detail.

Laakso, Ekaterina; Efimova, Sofya; Colalongo, Mattia; Kauranen, Pertti; Lahtinen, Katja; Napolitano, Emilio; Ruiz, Vanesa; Moškon, Jozé; Gaberšček, Miran; Park, Juyeon; Seitz, Steffen; Kallio, Tanja

Aging mechanisms of NMC811/Si-Graphite Li-ion batteries

Published in:
Journal of Power Sources

DOI:
[10.1016/j.jpowsour.2024.234159](https://doi.org/10.1016/j.jpowsour.2024.234159)

Published: 15/04/2024

Document Version
Publisher's PDF, also known as Version of record

Published under the following license:
CC BY

Please cite the original version:
Laakso, E., Efimova, S., Colalongo, M., Kauranen, P., Lahtinen, K., Napolitano, E., Ruiz, V., Moškon, J., Gaberšček, M., Park, J., Seitz, S., & Kallio, T. (2024). Aging mechanisms of NMC811/Si-Graphite Li-ion batteries. *Journal of Power Sources*, 599, Article 234159. <https://doi.org/10.1016/j.jpowsour.2024.234159>

This material is protected by copyright and other intellectual property rights, and duplication or sale of all or part of any of the repository collections is not permitted, except that material may be duplicated by you for your research use or educational purposes in electronic or print form. You must obtain permission for any other use. Electronic or print copies may not be offered, whether for sale or otherwise to anyone who is not an authorised user.



Aging mechanisms of NMC811/Si-Graphite Li-ion batteries

Ekaterina Laakso^{a,b}, Sofya Efimova^{a,c}, Mattia Colalongo^{a,d}, Pertti Kauranen^{a,b},
Katja Lahtinen^{a,e}, Emilio Napolitano^{f,g}, Vanesa Ruiz^{g,h}, Jozé Moškonⁱ, Miran Gaberščekⁱ,
Juyeon Park^j, Steffen Seitz^k, Tanja Kallio^{a,*}

^a Research Group of Electrochemical Energy Conversion and Storage, Department of Chemistry and Materials Science, School of Chemical Engineering, Aalto University, P.O. Box 16100, FI-00076, Finland

^b LUT University, Yliopistonkatu 34, 53850, Lappeenranta, Finland

^c Laboratoire MATIM, Université de Reims Champagne-Ardenne, 51100, Reims, France

^d European Synchrotron Radiation Facility, 71 Avenue des Martyrs, Grenoble, 38000, France

^e Department of Chemistry-The Ångström Laboratory, Uppsala University, Lägerhyddsvägen 1, Uppsala, 75121, Sweden

^f TOFWERK AG, Schorenstrasse 39, 3645, Thun, Switzerland

^g European Commission, Joint Research Centre (JRC) Petten, Netherlands

^h E-magyB.V., Bijlestaal 54a, 1721 PW, Broek op Langedijk, Netherlands

ⁱ National Institute of Chemistry, Department of Materials Chemistry, Hajdrihova 19, 1000, Ljubljana, Slovenia

^j National Physical Laboratory (NPL), Hampton Road, Teddington, TW11 0LW, United Kingdom

^k Die Physikalisch-Technische Bundesanstalt, GermanycPhysikalisch-Technische Bundesanstalt, D-38116, Braunschweig, Germany

HIGHLIGHTS

- Cycling and post-mortem analysis of Li batteries
- Comprehensive analysis of electrodes from fresh and cycle aged cells
- Temperature and state-of-health degradation dependence of Li batteries
- Key aging mechanisms have been discussed

ARTICLE INFO

Keywords:

Lithium-ion battery
NMC
Ageing
Degradation
Electrochemical impedance spectroscopy
Post-mortem study
State-of-health

ABSTRACT

Electrode degradation processes at various Li-ion batteries' state-of-health (SoH 100 %, 80 %, 50 %, and 30 %) and cycling temperatures (5 °C, 23 °C, and 45 °C) were investigated. For this purpose, the standard format of Li-ion cylindrical 18,650 batteries with Si-Graphite negative and LiNi_{0.8}Co_{0.1}Mn_{0.1}O₂ (NMC811) positive electrodes were cycled with registering battery parameters and the electrochemical impedance spectrum were recorded after every 200 cycles. Once reaching their end-of-life, electrodes from cycled batteries were subjected to post-mortem analysis. NMC811 positive electrode was observed to crack during the charge and discharge processes, suffered by irreversible phase transition, transition metal dissolution, cathode electrolyte interphase growth, and cation mixing. The Si-Graphite negative electrode material was also affected by crack formation, layer exfoliation, solid electrolyte interphase (SEI) recompositing, Li dendrite growth, transition metal contamination, and Si dissolution. Degradation of components leads to an increase of the contact resistance, Li⁺ diffusion limitations, reduction of active materials participating in Li-ion storage and, as a result, capacity fade that finally rendered the battery utilization unfeasible. Degradation processes can be detected by capacity fade and impedance growth of the full battery. High temperature accelerates electrode degradation processes when low temperature leads to SEI and Li dendrite growth.

* Corresponding author.

E-mail address: tanja.kallio@aalto.fi (T. Kallio).

<https://doi.org/10.1016/j.jpowsour.2024.234159>

Received 29 September 2023; Received in revised form 2 January 2024; Accepted 28 January 2024

Available online 18 February 2024

0378-7753/© 2024 The Authors. Published by Elsevier B.V. This is an open access article under the CC BY license (<http://creativecommons.org/licenses/by/4.0/>).

1. Introduction

Li-ion batteries are types of rechargeable batteries, whose prototype was discovered by Akira Yoshino et al. in 1985 [1,2]. They have become more popular and attractive in recent decades and nowadays are commonly used for the portable electronics, electric tools and electric vehicles [3]. Li-ion batteries have many advantages comparing to other energy courses: a high energy density, no memory effect, and low self-discharge [4]. However, they also present to be a safety hazard, as they contain flammable electrolytes, and in a case of damage or incorrect charging explosions and fires can happens [5]. Performance, durability, cost, and safety characteristics vary across the various Li-ion battery chemistries, electrolyte compositions and cell designs [6].

1.1. Aging of Li batteries

Battery cycle life is depends on many different stress factors where are the most important are temperature, charge current, discharge current, and state-of-charge ranges (depth of discharge, DoD) [7]. Batteries are typically used not fully charged and discharged conditions in real-life applications such as electric cars, laptops, or smartphones. So, determining battery lifetime via full number of discharge cycles can be misleading. Another way of the lifetime calculation is using cumulative discharge counted as the total amount of charge stored by the battery during its operation lifetime. On the other side, battery degradation during storage (shelf-life degradation) depends on temperature of environment and battery state-of-charge (SoC). A combination of conditions when the battery is charged up to high SpC values (near 100 %) and storing at high temperatures (usually $>50\text{ }^{\circ}\text{C}$) can cause a sharp capacity drop and also can be a reason of gas generation. Low SoC level (10–25 %) and low temperatures allow to decelerate degradation of Li-ion batteries. The main processes leading to the battery degradation are parasitic reactions on electrodes, interphases, and electrolyte [8–12].

Cycle life degradation is strongly temperature-dependent, with a minimal degradation around $25\text{ }^{\circ}\text{C}$, increasing if stored or used above or below $25\text{ }^{\circ}\text{C}$ [13]. High state-of-charge levels and elevated temperatures (whether from electrochemical cycling (self-heating) or from ambient air) hasten capacity loss. The cell reactions and diffusion processes are typically the heat sources in a cell. Battery generates heat when in use, with typically higher self-heating occurring during the charge phase. Overcharging, high C-rates, and local inhomogeneity accelerate heat generation and can lead to dramatic battery degradation and thermal runaway [14]. To reduce temperature effects, batteries may be cooled, and this is of relevance for high levels of assembly (battery packs and battery systems as in electric vehicles). The most common degradation processes contributing to heat generation while increasing temperature also accelerates chemical reduction of electrolytes on the surface of negative electrode, chemical oxidation of electrolytes by the positive electrode, and thermal decomposition of electrolyte in both electrodes, and internal short circuit [14].

Elevated temperatures either in the positive or negative electrode led to accelerated cell degradation. The effect of elevated temperature on degradation is a multifunctional problem because positive and negative electrodes can interact with each other. Therefore, half-cell studies can be potentially misleading. Ronny Genieser et al. cycled NMC/graphite cells at $80\text{ }^{\circ}\text{C}$ with different electrolytes and observed that using a suitable electrolyte is extremely important [15]. Scientists also concluded that capacity fade and large resistance increase in the NMC/graphite cells were mainly related to the degradation in the positive electrode. However, they observed that the bulk structure of the positive electrode material was unchanged. The capacity loss was deducted to be caused by the loss of active lithium. Resistance increase was explained by the disintegration of secondary particles of NMC. This type of the particle damage led to the decomposition and reconstruction of the primary particles grain boundaries.

Aging processes happening during cycling of Li-ion batteries depend on battery chemistry, and because our research is focused on NMC/graphite cells with a liquid carbonate electrolyte, we will follow this type of batteries or related chemistries in further discussion.

1.2. Negative electrode degradation

In the state-of-art applications, graphite is known as the most used negative electrode material, and therefore its aging mechanisms have already been widely investigated. The reasons for the cell aging are the degradation of an active material structure during cycling, the degradation of non-active cell components and continuous restructuring of the solid electrolyte interphase (SEI), which is discussed more detail in the next chapter. Lithium insertion into graphite can cause a 10 % volume increase between graphene layers. Volume change can also result in particle cracking, graphite exfoliation, or contact loss between the active electrode material and electroconductive additives, between the current collector and active material, between the binder and conductive additives, and between the current collector and binder [16]. Furthermore, fluorine-containing compounds such as LiPF_6 electrolyte salt or PVDF binder react with the negative electrode forming LiF [17]. Current collector corrosion can occur if the potential of the negative electrode rises to too high potentials vs $\text{Li}|\text{Li}^+$ or if a current collector is exposed to reactions with electrolyte components. As a result, electric and mechanical contact between the current collector and electrode material is lost. Volume changes of the active material and current collector corrosion can both cause contact loss of material components within the electrode resulting in higher cell impedance. Rising impedance is connected to the capacity and power fade of the battery [18].

1.3. Surface electrolyte interphase performance

Positive and negative electrodes are covered with interphase layers which are formed within the few first charging and discharging cycles from electrolyte and electrode species and influence to diffusion and redox processes [19]. Main species in a freshly formed SEI are LiF and lithium ethylene decarbonate. During aging, more complicated organic species, Li_2O , Li_2CO_3 , HF , C_2H_4 , PF_6 , H_2O , and other compounds are deposited on a negative electrode surface. The SEI layer works for protection for the electrolyte components from following reduction and preventing electrode from oxidation (corrosion) while letting lithium ions flow through [20]. The SEI components play roles of ionic conductor and electronic insulator [21]. High cell voltages typically exceed the window of electrochemical stability of the electrolyte components. Capacity fade is related to the SEI layer growth and decomposition which can occur during the whole lifetime of the cell, and impedance rise is mainly attributed to the increase of resistive components in the SEI layer. Inorganic salts are especially detrimental for impedance, and they are replacing organic components of CEI with aging. High voltages on graphite surface can cause the reduction of the electrolyte provoking SEI growth [19]. SEI layer formed under special operation conditions, archives a fixed thickness and composition after the first few charging and discharging cycles allowing the battery to be operated for years. Nonetheless, operation outside parameters used for SEI formation can lead to accelerating of battery degradation via several reactions [22]. Simultaneous to the flow of Li-ions through the SEI, several charged and neutral species may also diffuse through or into the SEI. For instance, transition metal migration from positive electrodes can cause SEI layer growth and contamination affecting Li diffusion and protection of the negative electrode [23].

1.4. Li plating

A small difference between the intercalation potential of graphite and metallic lithium exposes the possibility of lithium plating which occurs if potential below 0 V vs $\text{Li}|\text{Li}^+$ graphite is applied to negative

electrode. Lithium growth is a processes limited by reactions at the electrode/electrolyte interface in macro-scale, when the local reaction rate is limited by diffusion processes within the solid state interface in micro-scale [24]. It is supposed that dissimilar transport of positive and negative ions in an interfaces can cause dendrite formation and Li plating [25], and low temperatures lead to increasing of this difference in diffusion of lithium ions in the electrolyte. Dissimilar transport of ions increases the chance of lithium plating and further lithium dendrite upgrowth during charging. However, lithium plating can be also observed at higher temperatures if a cell has poor capacity balance between positive and negative electrodes or geometric misfits. Other factors increasing the risk of lithium plating are high cycling currents and high state-of-charge (SoC). Lithium plating causes capacity loss, impedance rise, and serious safety hazards due to dendrite upgrowth which can cause short circuit in the battery [26].

1.5. Positive electrode degradation

Family of lithiated transition metal oxides LiMO_2 where M can be Ni, Co, Mn, Al in different ratios is a wide set of materials with high capacity, stability, and power for the use as Li battery positive electrode materials. $\text{LiNi}_{0.8}\text{Co}_{0.1}\text{Mn}_{0.1}\text{O}_2$ (NMC811) is one of the most common materials from this family and it is widely use in different Li battery applications. NMC materials exhibit promising attributes for demanding applications and their aging mechanisms have been extensively studied in recent years. However, scientists are still uncertain which aging mechanism is the most crucial for cell performance [27].

Degradation of the cell is also caused by unwanted structural and chemical changes in the positive electrode. These changes may induce oxidation of the electrode components, migration of aging products to the negative electrode, decay of conductive particles, decomposition of the binder, corrosion of the current collectors, and passivating cathode electrolyte interphase (CEI) on the surface of an active material. The aging of an active material can be induced by phase transitions, structural disordering, microcracking, cation mixing, and dissolution [23, 27]. Structural disordering and phase transitions during cycling are considered to affect crystal lattice which results in hindering Li-ion diffusion.

1.5.1. Positive electrode volume change and cracking

Lithiation/delithiation of an active material leads to changes in volume also in the positive electrode side. It was suggested that the increasing of the c-axis is caused by a repulsive force originated from positively charged transition metal slabs in a highly lithiated state. S. Hwang et al. suggested that the a-axis of the NMC811 lattice decreases when voltage rises up to 4.3 V and remains almost stable at potentials from 4.3 V to 4.8 V [28]. Volume change at unit cell level induces mechanical stress and strain on the oxide particles which can lead to particle cracking. However, the addition of manganese or/and aluminum dopant is reported to help by stabilizing the structure and decreasing the total volume change during cyclic aging. Therefore, lithium nickel cobalt oxides doped with Al, Zr, Mo, Mn, etc., have better cycle life compared to undoped materials [29]. Cracking may cause contact losses between the active and non-active electrode components, which can be measured as an increased impedance. Mechanical degradation can also be an after effect of chemical degradation.

1.5.2. Ni^{4+} reactivity

One of the reasons why Ni-rich positive electrode materials have higher capacity comparing with LCO (LiCoO_2) is a possibility to proceed two reactions (Equation (1), (2)).



Reaction (1) is the main one and reaction (2) takes place at high

potentials. Recognizing of real oxidation state of each atom is not possible in the crystal lattice structure. Yet, with Li-ion deintercalation at high SoC crystal of active material tends to release oxygen or form NiO_2 phase to reduce oxidation state of $\text{Li}_{1-x}\text{NiO}_2$ component [27]. This process causes many degradation mechanisms of Li batteries. For example, Ni^{4+} readily reacts with the electrolyte, creating all sorts of decomposition products such as HF, CO_2 , CO, O_2 , organic compounds, fluorine and phosphorus derivatives, etc. [31]. The formation of new phases leads to the formation of cracks that allow penetration of electrolyte and decay products into the material. There is also a problem with the formation of oxygen, which is released from NiO_2 and reacts with the electrolyte facilitating electrolyte decomposition.

Muto et al. found that amount of inactive Ni^{2+} and Ni^{3+} in an electrode affects capacity fade [32]. The harmful decomposition can be explained by the formation of reactive Ni^{4+} at the delithiation state which reacts with the electrolyte species, leading to the electrode and electrolyte damage. Lattice parameter contraction caused by Ni^{4+} related irreversible phase transitions during operation can cause cracks along the grain boundaries inhibiting lithium diffusion and increasing impedance. Abraham et al. concluded the loss of oxygen from a positive electrode in reactions with an electrolyte [33]. Therefore, the oxidizing properties of the positive electrode against the electrolyte are an especially important aging factor. Additionally, the formation of the rock-salt sub-surface structure decreases Li-ion conductivity increasing in the surface impedance. The cell performance of Ni-rich NMC electrodes suffers from capacity fade caused by the ongoing decomposition of the electrolyte and structural changes at high potential, damaging the crystal structure and reducing the cycling and thermal stability.

1.5.3. Transition metal dissolution

The dissolution of NMC materials leads to several aging mechanisms including disproportionation reactions, acid corrosion, and transition metal ions dissolution. Dissolved transition metals can then migrate across the electrolyte and reduce on the negative electrode. In addition, the dissolution of NMC decreases Li^+ insertion sites. Higher voltages accelerate the dissolution of the transition metals because rapid electrolyte decomposition leads to the release of more acidic components. Also, the dissolution of NMC leads to the production of resistive MeF_x on the surface of NMC particles. Ochida et al. reported that de-intercalation and intercalation reactions of Li^+ at the graphite surface are retarded by manganese ions in the electrolyte [34]. Even if the electrolyte solution contains additives such as vinylene carbonate, vinylethylene carbonate, and fluoroethylene carbonate – which are known to form a strong passivating surface film on the graphite surface – Mn ions penetrate through the films leading to the deposition of Mn on the graphite surface.

1.5.4. Cathode electrolyte interphase

The CEI is formed on the surface of a positive electrode during cycling and consists of inorganic salts, transition metals and lithium ions, small number of organic compounds and other components [35]. Thickness of the CEI can vary from few nm to few micrometers depending on chemistry, SoH and cycling parameters. CEI is originated from Li_2CO_3 and LiOH which exist on positive electrode surface after contact with ambient CO_2 and H_2O . These species particularly react with an electrolyte as well as its decomposition products such as HF, CO, O_2 , etc., forming inorganic Li-containing materials like LiF and LiPO_xF_y . The CEI protects the surface of an active material from further reactions with the electrolyte and participates in the diffusion of lithium ions. CEI decomposition is the result of the electrolyte attack with a damaged active material, leading to excessive CEI growth and significant impedance increase which accompanies battery aging [36,37]. During battery operation, the CEI is growing with accumulation of oxidized and disproportionated oxides and salts of transition metals, which form an insulating layer and prevent lithium diffusion. This interface between electrode and electrolyte degrades rate capability and increases

impedance while its reformation consumes active lithium. In general, CEI aging is accelerated by high SoC, temperature increase and high cycling rates [38].

1.6. Degradation mechanism in the electrolyte

Electrolyte decomposition with the presence of charged positive material and lithiated graphite leads to CO_2 and HF evolution. High temperature and high voltage can enhance CO_2 gas evolution. It has been found that the presence of Li_2CO_3 greatly enhances the formation of CO_2 . Side reactions of lithium with moisture trace and CO_2 in the electrolyte can lead to the formation of LiOH and Li_2CO_3 . Gas evolution is understood as a life-limiting factor only when cells are maintained at high temperatures and SoC [19].

1.7. Motivation of the research

Despite the large number of scientific research related to the aging of Li-ion batteries, this topic is still relevant as most of the works consider only isolated problems in the degradation of Li-ion battery components without reviewing the battery as a whole. On the other hand, existing studies of full Li-ion batteries are mainly limited to consider the behavior of these full Li-ion batteries without analyzing the individual components. As a result, the relationships between the various aging effects of individual components and the battery as a whole were not fully understood. Another challenge comes from complicity of Li batteries where each component effect all others and battery as a whole. However, articles related to aging of Li battery cells are focused on separated aging mechanisms end/or components ignoring relationships among them.

In our research, we have investigated battery aging to different SoH (100 %, 80 %, 50 %, and 30 %) and at various temperatures (5 °C, 23 °C, and 45 °C) as whole system using electrochemical impedance spectroscopy (EIS) of the full cells and performed postmortem analysis of the electrodes extracted from the cycled cells using scanning electron microscopy (SEM), X-ray diffraction (XRD), rate capability tests and cyclic

voltammetry (CV) to investigate aging mechanisms and effect of temperature on battery cycling aging.

2. Experimental part

2.1. Aging of commercial cells

The 18,650 format cells (Fig. 1a) with NMC811 and graphite electrodes were used in our work. The nominal capacity of the cells was 3000 mA h and the nominal voltage, 3.6 V. According to cell specifications, the maximum charge voltage was 4.2 V, the maximum charge current, 4 A, and the maximum discharge current, 20 A. Operating temperature range given by the manufacturer was from 0 to 50 °C for the charge and -20 to 75 °C for the discharge.

2.2. Full battery degradation protocol cycling

In this study, five identical batteries had been cycled in a climate-controlled chamber at set temperature with a Maccor 4300 battery testing station. The details of the cycling protocol had been reported in our earlier publication [39]. Basically, the batteries were CC charged to 4.2 V at 4.0 A (1.33 C) and CV charged at 4.2 V to a cut of current of 100 mA, followed by a 4 A discharge to 3.0 V at the selected cycling temperature. The batteries were periodically (every 20 to 200 cycles) brought to room temperature for capacity measurement and EIS characterization. The capacity was measured at a lower current of 1.25 A (0.4 C) and the SoH was determined as the remaining capacity divided by the initial capacity of the battery cell at 1.25 A current. EIS was recorded at six different state-of-charge (SoC) using the parameters given in Table S1. However, as the SoC adjustment is time consuming and not feasible for practical testing purposes, only EIS spectra at full 100 % SoC were used in further analyses.

Temperature of cycling was 5 °C, 23 °C and 45 °C and cycling was performed down to various SoH. The exact values for the cells were 28.6 % SoH cycled at temperature 45 °C (Cell #5), 50.0 % SoH cycled at temperature 45 °C (Cell #6), 79.9 % SoH cycled at temperature 45 °C

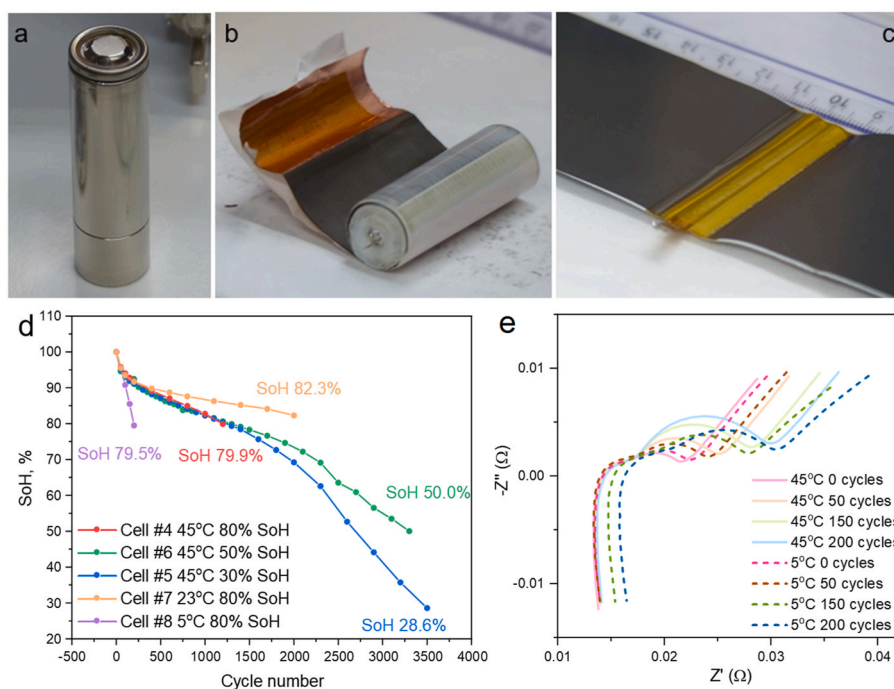


Fig. 1. (a) A as received cell without a polymeric jacket and (b, c) a disassembled cell. Photos demonstrate (b) a negative electrode and (c) positive electrode. (d) SoH vs cycles of five cells cycled down to various SoH values at different temperatures as indicated in the legend, the values given in the figure indicate the actual SoH at the end of their cycling; (e) EIS profiles measured every 50–100 cycles for the full Li-ion battery cells cycled to 80 % SoH for 200 cycles at 45 °C and 5 °C.

(Cell #4), 82.3 % SoH cycled at temperature at 23 °C (Cell #7), 79.5 % SoH cycled at temperature 5 °C (Cell #8) cycled at 5 °C (Fig. 1d). Additionally, a non-cycled battery with SoH 100 % (Cell #1) stored at room temperature was investigated. For further discussion, we will identify these batteries using their rounded-up SoH at the end of the aging process – 30 %, 50 %, 80 %, and 100 %, respectively.

2.3. Full battery degradation protocol opening

Before the disassembling, the cylindrical 18,650 cells were discharged at a constant current of 0.6 A down to 2.0 V. The plastic wrapping was then removed, and a groove (depth of 0.11–0.12 mm) was cut on the metallic surface of the cylindrical case using a lathe-cutting machine to make opening easier. The small engraving depth was sufficient to guarantee the seal of an 18,650 cell and at the same time necessary to facilitate the opening and removal processes of the cylindrical case to expose the jelly roll. Subsequent opening, disassembling, and sample harvesting processes were performed inside an argon-filled glove box ($O_2 < 0.1$ ppm; $H_2O < 0.1$ ppm). The cell was opened, and, after extracting the jelly roll (Fig. 1b and c), positive and negative electrode foils were separated and cut into pieces of circa 60×50 mm². Each aliquot was stored in a transparent plastic bag and loaded inside a stainless-steel vacuum tube to guarantee protection against moisture and air during shipment because opening cells and characterization of the electrode materials were performed in different institutions. A glove box ($O_2 < 0.1$ ppm; $H_2O < 0.1$ ppm) was used for storage and handling of the electrode samples. The cut electrode samples were used for further characterization and electrochemical tests.

2.3.1. Scanning electron microscopy

Scanning electron microscopy was used to investigate the topography and particle size of the electrodes. In this work, JEOL JIB-4700F scanning electron microscope featured with a hybrid conical objective lens, the GENTLEBEAM™ mode, and an in-lens detector system was used to perform measurements. An accelerating voltage of 5.0 kV was used. The elemental composition and distribution of the electrodes were measured by an Energy Dispersive X-ray (EDX) spectroscopy using the same equipment with an accelerating voltage of 15.0 kV.

For sample preparation, small pieces (~5 mm × 5 mm) were cut from the original electrodes, positioned on a SEM stub with double-sided adhesive carbon tape and transferred from the glovebox to the SEM sample chamber in argon atmosphere by using a hermetic sample holder JEOL SM-71190TV.

The particle size distribution was measured and calculated with the use of ImageJ program [40] choosing the largest length of secondary and primary particles. Results were drowned by Origin Lab software using tool “Violin with box” which displays number of particles with definite particle size as function of graph’s width vs. size of particles.

2.4. Powder X-ray diffraction

The powder XRD characterization method was used to investigate the crystal structure of the samples. XRD measurements were performed with PANalytical X’Pert Pro MPD α -1 with Cu X-ray source and $K_{\alpha 1}$ monochromator with a working voltage of 45 kV and current of 40 mA. The corresponding wavelength of the X-ray was 0.15406 nm. The measurement was performed in Bragg-Brentano geometry and angular range was 10–105 $2\theta^\circ$, the step size 0.0131303 $2\theta^\circ$ and the scan speed 0.0167262 $^\circ \cdot s^{-1}$. A model PIXcel1D detector was used, and the sample spinner was turned on. The patterns were interpreted using the Match software.

2.5. X-ray Absorption Spectroscopy

The X-ray Absorption Spectroscopy (XAS) data were gathered at the Balder beamline in MaxIV (Lund, Sweden) [41]. The cycled electrodes

were opened in an argon filled glovebox and mounted inside a double-sided Kapton window chamber to avoid any air contamination. The spectra normalization was performed using Athena software from the Demeter package [42]. Values of edge-step were extracted by the difference between post-edge line and pre-edge line values and averaged over 4 spectra per sample. Error bars were calculated by the standard deviation of each spectra edge-step value.

2.6. Coin cell assembly

Hohsen XR2016 coin cells were assembled in the glovebox for the charge/discharge galvanostatic testing of extracted negative electrode materials in a half-cell configuration with a lithium counter electrode. Electrode materials were cut into a circular shape (diameter of 18 mm) and placed under a glass fiber separator (Whatman GF/A, thickness 0.26 mm, diameter 19 mm). 200 μ l of 1 M lithium hexafluorophosphate (LiPF₆ dissolved in 1:1 ethylene carbonate and dimethyl carbonate, Sigma Aldrich) were used as an electrolyte. The lithium metal foil (0.75 mm thick, 99.9 %, Alfa Aesar) was cut into a circular shape by using an ECC-Li Punch tool (diameter of 17 mm) and used as a counter electrode.

2.7. Three-electrode cell assembling

Three-electrode cells with Li counter and reference electrodes were assembled in an argon-filled glovebox using EL-Cells. The working electrode was extracted electrode material cut into a circular shape (diameter of 18 mm). The reference electrode was a lithium wire (diameter of 1 mm, 99.9 %, Alfa-Aesar) and the counter electrode was lithium metal foil (0.75 mm thick, 19 mm in diameter, 99.9 %, Alfa-Aesar). The separator (glass fiber D18 mm x h1.5 5 mm EL-Cell ECC1-01-0012-C/X) and 600 μ l of 1 M lithium hexafluorophosphate electrolyte (LiPF₆ dissolved in 1:1 ethylene carbonate and dimethyl carbonate, Sigma Aldrich) were also used for the cell.

Similar architecture was used for the charge/discharge galvanostatic testing of extracted positive electrode materials in half-cell configuration, but no reference electrode was installed when a plastic cap sealed the reference electrode port.

2.8. Charge/discharge galvanostatic tests

Rate capability tests were performed using the LAND CT2001A Battery Testing System. Assembled coin cells were allowed to stabilize for 20 h before the measurements. The mass of active material in the positive electrode was 0.041 g while the corresponding number in the negative electrode was 0.022 g. Initial conditioning step was performed with one cycle of 0.03 C and three cycles of 0.1 C. In a case of fresh batteries, it is important to perform SEI/CEI formation, but in case of the investigated materials, SEI has been already formed. Yet, conditioning steps were still important, at first, to make measurement conditions similar with ones ordinary used, and, at second, to form SEI/CEI in a case of surface damaged during cycling and/or opening cells. C-rates of charge and discharge were kept the same during conditioning cycles. The voltage range was between 3.0 and 4.4 V for positive electrode measurements and between 0.01 and 1.0 V for negative electrode measurements. After conditioning cycles, the measurement was continued by maintaining the charging C-rate at 0.2 C varying the discharge C-rate from 0.2 C through 0.5 C, 1.0 C, 2.0 C, 4.0 C, and 5.0 C measuring three cycles per each C-rate for a positive electrode and vice versa for a negative electrode. After this, three more 0.2 C cycles were performed to obtain experimental information about the cyclability properties of the materials. More details of charge/discharge galvanostatic testing are given in Table S2.

2.9. Cyclic voltammetry

EL-Cells with three-electrode configurations were used for the CV

measurements. These measurements were performed with a Biologic MPG-205 and with an EC-Lab V11.31 software. The mass of active material in the positive electrode was 0.041 g while the corresponding number in the negative electrode was 0.022 g. The relaxation time between the cell assembly and measurement was set to 20 h. The potential window was set between 3.0 and 4.4 V vs. $\text{Li}|\text{Li}^+$ for a positive electrode and 0.01–1 V vs. $\text{Li}|\text{Li}^+$ for a negative electrode. Scan rates of 20, 50, and $100 \mu\text{V s}^{-1}$ were used for both electrodes. Cells were cycled three times with each scan rate and the most repeatable results were chosen.

3. Results and discussion

The idea of research was to investigate aging processes met at different SoH as well as effect of low and high temperature on cycling aging of full batteries. For this reason, 3 batteries were cycled down to 80 % SoH, 50 % SoH and 30 % SoH at 45 °C temperature and 2 batteries were cycled down to 80 % SoH at 23 °C and 5 °C temperatures. During cycling, every 50–200 cycles an EIS spectrum was recorded. After aging, these 5 batteries and one battery with 100 % SoH were opened and electrodes were characterized.

3.1. Effect of cycling on capacity and impedance of full batteries

All the cells cycled at 45 °C demonstrate similar degradation rate up to 1500 cycles after which the performance begins to deviate (Fig. 1d). All the cells #4, #5 and #6 were cycled under the same conditions, but we noticed their different behavior after ~1500 cycles. Degradation rate of Cell #5 was much higher compared to the Cell #6, and thus with similar number of cycles they reached different SoH level: SoH of the Cell #6 after 3300 cycles was 50.0 % and SoH of the Cell #5 after 3500 cycles was 28.6 %. It can be related to local inhomogeneities of active materials and other cell parts which have different degradation speed.

Fig. 1e and Fig. S1 demonstrate impedance spectra recorded for the samples cycled at 45 °C and 5 °C. During cycling at 45 °C (Fig. S1), few changes are observed: battery ohmic resistance (can be roughly estimated from Z' value at point of $Z'' = 0$), direct current resistance (can be roughly estimated from Z' value at point related to the low frequency end of semicircle), Warburg impedances (can be roughly estimated from the angle of the tail) were increasing, and diffusion properties (can be roughly estimated from Z' value at the point related to the top of the semicircle) were decreasing [43]. With increasing number of cycles this degradation process accelerated significantly. Detailed analysis of impedance spectra of these samples was done in our previous research [39]. Decreasing temperature to 5 °C leads to few very interesting effects (Fig. 1e). Most important is that the impedance spectra of both samples at the same cycles were relatively similar and did not depend on the SoH level. It indicates different mechanisms affecting at low temperature battery aging and on impedance growth. At the same time, ohmic resistance, and Warburg impedance were increasing faster for the lower temperature, direct current resistance change was similar for both samples and the diffusion properties tended to have faster decreased at the higher temperature.

To investigate aging processes in more detail, the positive and negative electrodes were investigated separately by SEM, XRD and electrochemical testing.

3.2. Positive electrodes

Samples of the positive electrodes extracted from 6 cells described above were black stuck substance coated on a “silver” colored metallic foil. Visually, all positive electrode samples appeared similar and seemed to be undamaged. It was not possible to scratch or remove film from the foil.

3.2.1. Morphology

Aging of the positive electrode was investigated by comparing SEM

measurements of the samples from the fresh and aged batteries regarding morphology and particle size. The magnified images of the positive electrodes were presented in Fig. 2a and b and in Fig. S2 to visualize changes in the structure induced by the differences in the SoH and aging temperatures. The positive electrode active materials were observed to consist of spherical particles which seem to have a prominent secondary structure in all the samples whereas the primary particles were more clearly visible for the material from the uncycled battery. After cycling, the surfaces of the electrodes become more degraded as evidenced by the appearance of additional pores and inhomogeneities. Most of the particles in the electrodes from the 80 % SoH aged cells at different temperatures appeared relatively unchanged. Those from the cells with 50 % SoH and especially 30 % SoH had some visible surface changes such as cracks, isolated particles, contaminations from the electrolyte, but those were not dramatic. For the aged samples, cracks on the surface were also observed with a low magnification. Also, small slits between the particles and the surrounding binder were observed, which plausible result from the volume changes during the delithiation/lithiation processes.

The mean secondary particle size was ~7–9 μm as seen in the particle size distribution diagrams in Fig. 2c. The primary particle size was approximately 0.6 μm . The secondary particle size increased with the decreasing SoH as shown in Fig. S3, and the dependence was close to linear. It could be attributed to the electrode degradation of active material layers, loosing connection between the electrode particles, crack formation and CEI growth. Aging at different temperatures did not affect the size distribution largely. However, for the sample aged at 23 °C, the number of very small particles was high compared to the samples aged at 45 °C or 5 °C originating apparently from cracking of the larger particles. The cycle number was an important difference between these samples, and that was higher for the sample aged at 23 °C. Hence, to summarize, two important effects detected in the electrodes was noticed: (1) increasing SoH leads to exfoliation of the active materials leading to increasing of particle size in relatively linear manner, and a high number of the cycles lead to increasing crack formation. Cracks increase the internal resistance of the electrode and cause capacity fade due to the loss of electrical contact. Cracking is related to lithium intercalation/deintercalation reactions as well as phase transitions during cycling which expand and contract the distance between the transition metal oxide layers in the active material lattice. The crack formation facilitates electrolyte penetration into the active material structure resulting in side reactions [44].

3.2.2. Atomic composition

The atomic compositions of the positive electrode electrodes were determined with EDX analysis. Table S3 presented the distribution of all observed elements for the aged and fresh samples. Mn, Co, and Ni transition metals were found in all the samples. Based on their ratio the investigated material was concluded NMC811 close to the $\text{LiNi}_{0.82}\text{Co}_{0.11}\text{Mn}_{0.7}\text{O}_2$ formula. Traces of Zr verified the presence of Zr doping or coating which is one of the most promising additive materials for improving the electrochemical properties of the NMC811 active material family [27]. It should be noted that the EDX analysis was limited by three important factors. First, the depth detection depth was close to the μm scale and consequently, only the materials surfaces could be investigated with this method. Level of the systematic error was the second factor which was near 1 at. % or more, depending on the equipment. The relative error was comparatively low and hence in the case of a series of similar samples were measured in a sequential manner. However, the results were reliable even if the element concentration was below the systematic error level. Thirdly, only a limited part of the whole samples could be measured in practice. Electrodes can be very inhomogeneous even at the scale of secondary particle size, and the direction of the X-ray beam to the electrode surface and particles affect results as well. Electrodes are aging differently in different parts of the cell demonstrating distinction of morphology, structure and

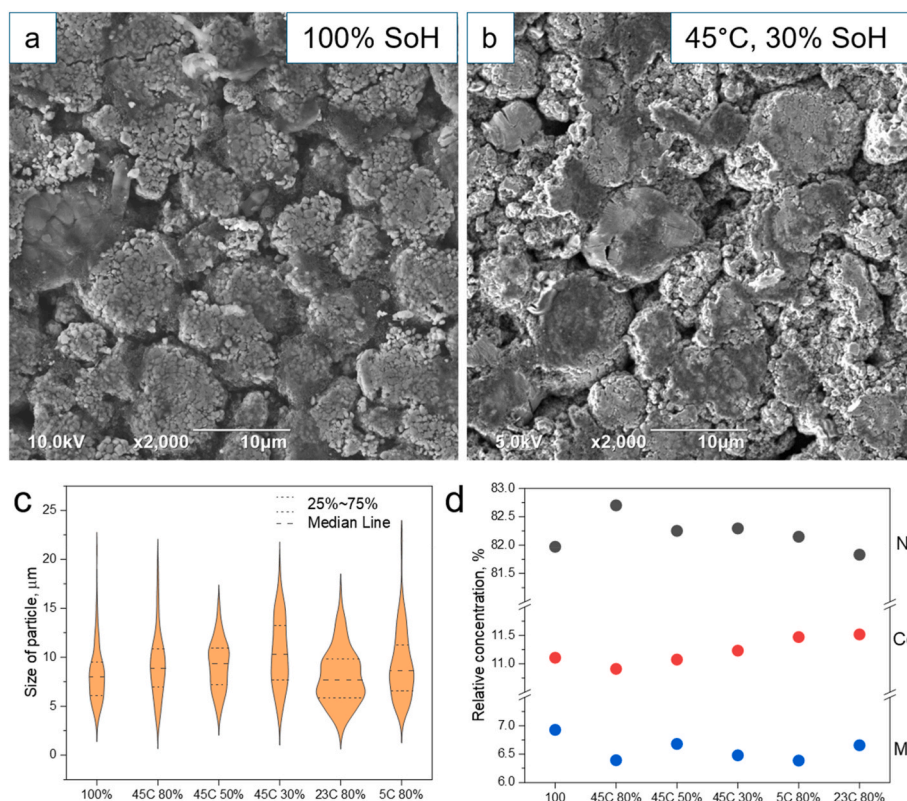


Fig. 2. The SEM images 2000 \times magnified for the positive electrodes extracted from the cells (a) 100 % SoH and (b) 45 C, 30 % SoH. (c) The size distribution analysis of the positive electrode samples. Thickness of the orange bars is related to number of particles of corresponding size. (d) The relative content of Ni, Co, and Mn on the positive electrode surface calculated from the EDX analysis for the electrodes from the cells with the different SoH and aged at different temperatures (the sum of all the Ni, Co, and Mn atoms adds up to one).

electrochemical properties in inner and outer parts of the electrode in jellyrolls [45]. So microscopic and EDX study can have a considerable measurement error. To minimize this risk, at least three series of measurements were carried out for each electrode in this work. In Fig. 2d the relative content of Ni, Co, and Mn on the positive electrode surface (all Ni, Co and Mn atoms adds up to one) was demonstrated.

Based on the EDX analysis for the positive electrodes, the amounts of Ni, Co and Mn were noticed to be rather stable or varies only slightly with decreasing SoH and varying temperatures. Mn content was decreased, especially with decreasing SoH and was low also in the sample aged at 5 °C. Ni concentration also tended to decrease with the number of cycles. This was related to leaching of Ni and Mn from the positive electrode and their further deposition on the negative electrode. Mn is more susceptible to dissolution than Ni, when Co appears to be the most stable element in this system [30,46–48]. Samples taken from the cells 100 % SoH and 45 C° 80 % SoH were not in line, which can be related to complexity of measurements described above. We suggest that at low temperature leaching of the Mn was accelerating because of higher mobility of Mn under these conditions. For the cell aged at 23 °C and the one cycled down to 40 % SoH, the higher number of cycles can contribute to the Ni dissolution from the positive electrode.

Fluorine, phosphorus, and sulfur traces were found in all the positive electrode samples. While phosphorus and sulfur most probably originate from the electrolyte, fluorine can also be attributed to the binder. Absolute concentrations of fluorine and phosphorus had a tendency to decrease with the decreasing SoH level (see Fig. S4). Aging temperature seems to have little effect on the decrease of fluorine with decreasing SoH. We propose that most of the fluorine detected by the EDX method is from the binder. The amount of binder become lower with the decreasing SoH suggesting binder degradation. Moving from 100 % SoH to 30 % SoH, the absolute concentration of fluorine decreased almost 3

times from 7 at% to ~2.5 at%. As for phosphorus, it can originate only from the electrolyte. A slow decrease of the amount of this element was observed with the decreasing SoH. A dramatic drop was observed when aging at the temperature of 5 °C, which can be attributed to the CEI impoverishment on the positive electrode. This effect has not been shown for the CEI layer before, but it was investigated for SEI layer. High temperatures of SEI formation and battery operation promote thickening of SEI layer when low temperatures facilitate impoverishment of SEI [19,49]. Low temperature cycling can lead to local overpotential, which, in turn, provokes SEI growth and Li dendrite formation [35,50].

Carbon absolute concentration remained between 38 and 47 at%, and oxygen absolute concentration between 32 and 47 at.% for the fresh and aged samples. Small amounts of aluminum (0.15 at%) was found in the aged samples with 30 % and 50 % SoH aged at 45 °C and with 80 % SoH aged at 23 °C. We are suggesting that they originate from the separator and electrolyte. Al was also found on the separator surface facing the negative electrode, but some particles can be also on the positive electrode side. Sulfur atoms, also observed on positive electrode samples, can originate from the active material as sulphates are the most popular NMC811 precursors [51] or from the electrolyte as sulfur containing additives play important role in stabilizing of Li batteries [52].

3.2.3. Structural properties

XRD was used to investigate structural changes in the aged and fresh samples. Obtained diffractograms for the positive electrode materials were consistent with literature for typical NMC811 [53] indicating that the positive electrode materials belong to the $R\bar{3}m$ space group confirming $\text{LiNi}_{0.8}\text{Mn}_{0.1}\text{Co}_{0.1}\text{O}_2$ lithiated oxide. XRD results of the positive electrode samples were summarized in Fig. 3a and b and more XRD data can be found in Fig. S5.

Peaks in all patterns of the samples could be distinguished clearly

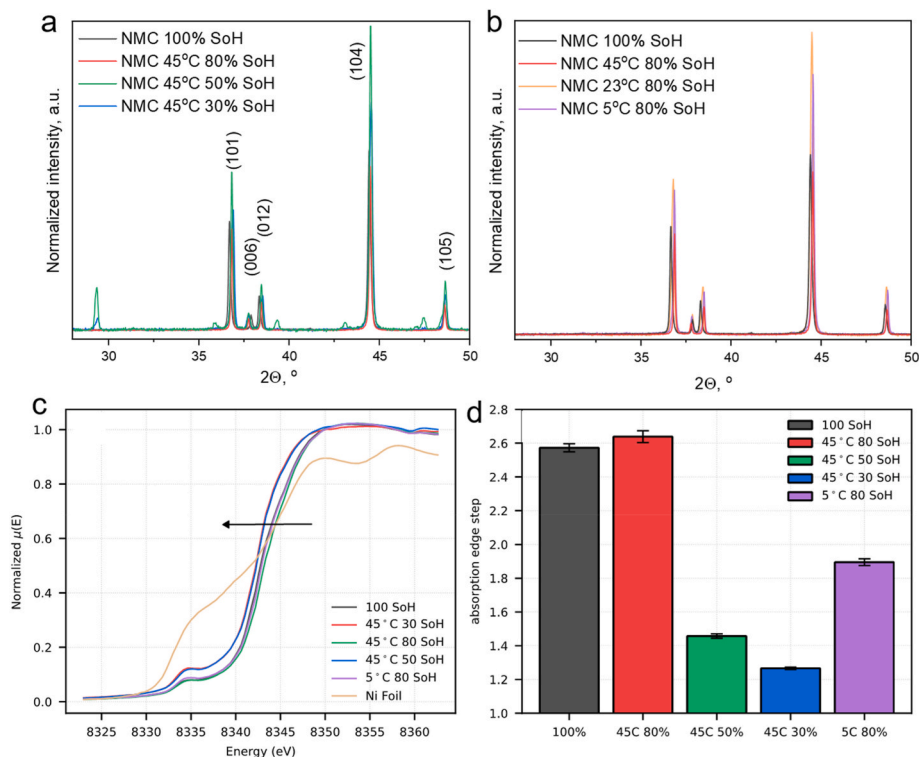


Fig. 3. Structural information of the aged electrode materials. Magnified diffractograms for the electrode materials from the cells (a) with the different SoH and (b) aged with different temperatures. (c) Ni K-edge spectra of Ni metal foil, 100 % SoH, 45 °C 80 % SoH, 45 °C 50 % SoH, 45 °C 30 % SoH, 23 °C 80 % SoH and 5 °C 80 % SoH. (d) Extracted edge-step values with the error bars over 4 measured spectra.

therefore indicating that the structures of fresh and aged samples are crystalline. The peak width increases with the decreasing SoH which is related to the decreasing crystallite size and confirms our statements about microcracks formation and exfoliation during cycling based on the SEM images. Few extra phases with peaks at $2\theta^\circ$: 26.6, 29.4, 35.9, 39.4, 43.1, 47.5, 57.4, 60.8, and 70.2 were observed for the materials from the cells with SoH of 50 % and 30 % but their nature was not clear. These can be related to the formation of Ni_3O_4 spinel [54], NiO rock-salt [55], LiF [44] or Li_2CO_3 [56,57] phases, and other species. The positive electrode from the cell cycled down to 50 % SoH was different from the others with a lower (104) peak and the highest intensity of the extra phase peaks. One explanation for this could be a local overpotential in this area where the electrode originates from confirming ununiform aging and degradation of the cells. XRD patterns for the electrodes cycled at different temperatures were relatively the same except for the sample aged at 23 °C. Its peaks were wider in comparison to the others which was ascribed to the higher number of cycles.

3.2.4. X-ray absorption spectroscopy

To understand the degradation process of the aged positive electrodes, Ni, Mn, and Co K-edges were investigated. As shown in Figs. 3c and 45 °C 50 % SoH and 45 °C 30 % SoH clearly show a shift to lower energies in the XANES spectra compared to 100 % SoH. Therefore, they do possess, partially, a lower oxidation state compared to the pristine material. There are two possible degradation mechanisms described in the literature which might justify a shift to lower energies upon cycling: i) Yu et al. observed that for cycled electrodes, both Ni and Mn undergo a shift to lower oxidation states compared to the pristine material and attributed its cause to a decrease of Li/transition metals ratio [58]. It is true that when Li^+ is de-intercalated from the host structure the transition metals will migrate in Li-sites impeding its re-intercalation upon discharge [59,60]. ii) It is also common in Ni-rich materials to incur in transition metals dissolution [61,62] which would also cause a reduction of the Ni, Mn and Co ions since their local environment will be

richer in Li^+ cations.

A reliable indicator to inspect whether metal corrosion is happening or not, is to examine the absorption k-edge step per each measured sample. Excluding in first approximation auto-absorption phenomenon for 120 μm thickness electrodes, the edge step is sensitive to the transition metal concentration and it is often used for quantitative analysis [63]. As shown in Fig. 3d, the edge jump of 45 °C 80 % SoH is similar to the 100 % SoH sample. However, for 45 °C 50 % SoH and even worse for 45 °C 30 % SoH, the edge step decreases drastically. The drop defines a loss in concentration for the specimen probed. Therefore, it is true that a drop in capacity for aged positive electrodes is driven by the transition metal migration in lithium sites, which permanently hinders the re-intercalation process of the lithium reducing the overall capacity every cycle, but in this case the degradation mechanism is rather induced by metal dissolution. Further to Ni element, Mn and Co were also investigated, as shown in Fig. S6, but both Co and Mn do not show a clear shift in lower oxidation states compared to the 100 % SoH sample. Furthermore, the difference in edge jump for Co and Mn is less pronounced compared to Ni, indicating that the main metal (Ni) is the one that has leached the most and more sensitive to the degradation of the material.

3.2.5. Electrochemical properties

To investigate the battery behavior of the extracted positive electrodes, rate capability measurements were carried out in half cells the voltage range of 3.0–4.4 V. The results were shown in Fig. 4. As expected, the capacity of the samples was decreasing with the increasing C-rate (Fig. 4a and b). At the low C-rates (0.03 C, 0.1 C, 0.2 C), electrochemical processes occur even if mass transfer is slow. That can limit electrochemical processes at the high C rates, and the amount of active material involved in the redox process decreases. 0.03 C was a conditioning cycle. For non-cycled batteries, the low C rate cycle is important for CEI/SEI formation. In our case, all the batteries were formatted, however, to follow typical cycling protocol and to form CEI/SEI layers in

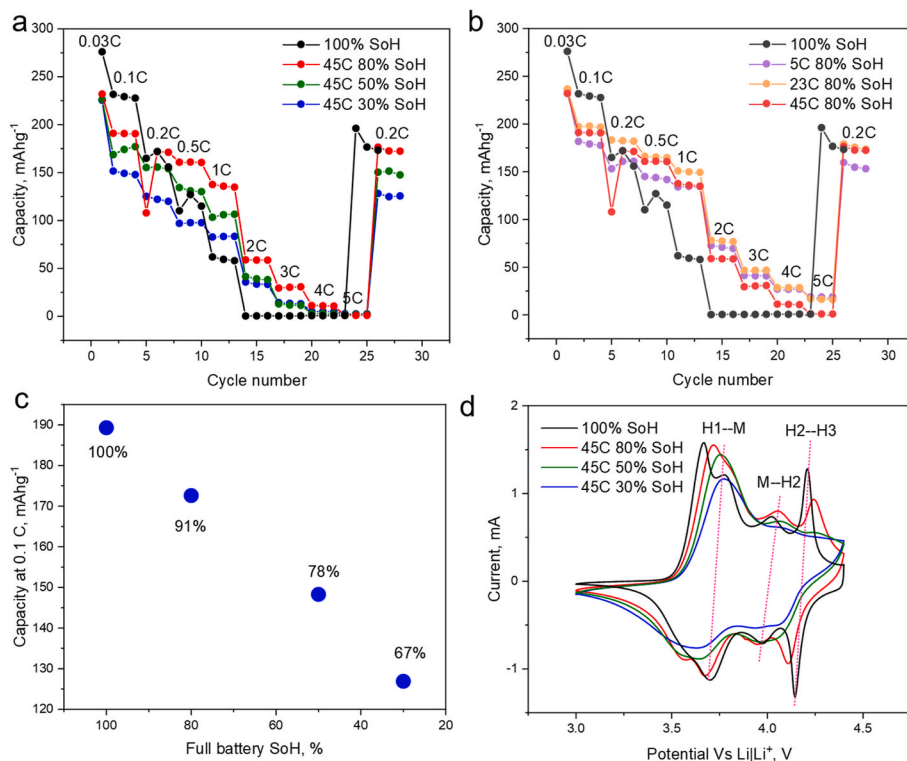


Fig. 4. The rate capability tests of the positive 1 electrodes from the cells (a) aged to the different SoH levels and (b) aged at different temperatures. (c) The capacities of the positive electrodes from the cells aged to the different SoH levels at the C -rate of 0.1 C. (d) CV curves of the positive electrodes ($20 \mu\text{V s}^{-1}$ scan rate in 3-electrode cell vs $\text{Li}|\text{Li}^+$) aged to the different SoH levels.

a case if it was damaged during opening and assembling testing cells, conditioning cycles were applied. The capacity at this C -rate correlates with the maximum capacity of the battery ($\sim 280 \text{ mA h g}^{-1}$). With the decreasing SoH of the cells, the positive electrode capacity drops down to 130 mA h g^{-1} which was slightly different for all the samples and related to the electrode degradation. The maximum capacity of the positive electrodes at 0.1 C linearly was decreased from 190 mA h g^{-1} to 130 mA h g^{-1} (67 % of the original capacity) with the decreasing SoH from 100 % to 30 % as shown in Fig. 4e. At 1 C the capacity first was increased from 60 mA h g^{-1} to 135 mA h g^{-1} and then decreased to 80 mA h g^{-1} with the decreasing SoH of the investigated batteries (Fig. S7a).

At the low C -rates, the capacity is limited by the amount of the positive electrode active material participating in the redox processes and a linear capacity fade shows its linear degradation accompanied by unwanted phase transitions, cation mixing, contact loss, Li loss, Ni/Co/Mn leaching, and other possible mechanism discussed in chapters 1.5–1.7. Our findings from SEM confirm crack formation result in contact loss while EDX data suggest Ni and Mn dissolution and binder degradation. Structural changes observed by XRD are related to irreversible phase transition, exfoliation of particles and cation mixing. Indirectly, signs of cyclable Li loss exist, which can be relocated in the SEI/CEI layers as LiF , Li_2CO_3 , or organic compounds. SEI formation and negative electrode degradation was discussed below in more detail. However, not only active material reactions limit capacity but mass and charge transfer can also play a role, and there are few important processes which can be limiting. Electron transport in electrodes is supported by conductive agent, and as discussed above, cracks, electrode, and conductive agent degradation lead to its decrease. Li^+ diffusion in solid state is affected by particle size, $\text{Ni}^{2+}/\text{Li}^+$ mixing, defects in crystals and charge transfer in CEI. It can also suffer from aging of negative electrodes caused by SEI growth and surface contamination. Li^+ transfer in an electrolyte is mostly limited by electrode 3D architecture including thickness and tortuosity, and this type of transfer is most important for

the rate capability behavior [64]. At high C -rates, behavior of the positive electrodes was not linearly (Fig. S7a) dependent on the SoH level. At 1C, capacity first was increased from $\sim 60 \text{ mA h g}^{-1}$ to $\sim 137 \text{ mA h g}^{-1}$ with decreasing SoH from 100 % to 80 % and then was decreased more linearly from 80 % to 30 % SoH. Similar effect has been found by Daubinger et al. [65] but potential reasons were not discussed. We suggest, that during first cycles, tortuosity of the electrodes undergoing changes so that more Li^+ pathways in the electrode open making the Li^+ diffusion more effective. This leads to higher rate capability values of the electrodes, but after 80 % SoH this effect becomes less important than active material degradation. Aging temperature does not affect rate capability of the electrodes, and the small differences can be related with inhomogeneity of the studied electrodes.

CV curves of the fresh samples in Fig. 4d, Fig. S7b, Fig. S8, and Fig. S9 demonstrate phase transition with peaks typical for NMC811 [27,29] at 20, 50, and $100 \mu\text{V s}^{-1}$ scan rates. With decreasing the scan rate from $100 \mu\text{V s}^{-1}$ to $50 \mu\text{V s}^{-1}$ and $20 \mu\text{V s}^{-1}$, the peak currents were proportionally decreased. The peaks are associated with electrochemical processes occurring at the electrode when the potential is applied. In the low-voltage region, ① (3.62 V) and ② (3.74 V) peaks correspond to the phase transitions between the initial hexagonal phase (H1) to the monoclinic phase (M). At the high-voltage regions, ③ (4.00 V) and ④ (4.17 V), the peaks correspond to the phase transitions between the monoclinic phase, second hexagonal (H2), and third hexagonal (H3) phases [66]. The M–H2 peak expresses formation of a second hexagonal phase that possesses fewer lithium atoms. The H2–H3 phase transitions in the potential range of 4.1 V–4.3 V are accompanied by the formation of a highly reactive Ni^{4+} and the further formation of HF, and oxygen loss [67]. The high potential leads to the formation of an irreversible rock-salt and spinel phases preventing Li^+ intercalation. The CV curves measured for the electrode with 100 % SoH and the electrode aged to 80 % SoH at 45°C demonstrate the presence of all described peaks at $100 \mu\text{V s}^{-1}$, $50 \mu\text{V s}^{-1}$, and $20 \mu\text{V s}^{-1}$. Reducing SoH to 50 % significantly reduces the height of the M–H2 and H2–H3 phase transition peaks,

especially at $100 \mu\text{V s}^{-1}$. Further reduction of the battery SoH to 30 % affects the positive electrode behavior so that the peaks diminish even more. It is related with decreasing amount of the active material participating in redox processes, because of such ageing processes as metal leaching, irreversible phase transition and cation mixing [68].

Fig. S9 depicted the CV curves normalized to the mass and scan rate. A decrease in the battery SoH level leads to a shift of the peaks on the charge curve to the higher potentials and the peaks on the discharge curve to the lower potentials, and this effect is more pronounced for higher scan rates. The peaks on the CV curve broaden as the battery SoH level decreases and some of them become undefined. Difference in potentials between the peaks on the charge and discharge CV curves depends on Li^+ diffusion in the active material crystal lattice. However, thickness and porosity of an electrode can lead to local potential drop and additional diffusion limitation which also affect peak position [69]. Li^+ diffusion in the bulk, as discussed above, can be limited by cation mixing, defect formation and surface contamination. Shifts and broadenings of the peaks indicates deterioration of the Li^+ bulk diffusion from 80 % to 30 % SoH and a decrease in the crystallinity of the positive electrode active material as confirmed by XRD results (Fig. 3).

Fig. 4d demonstrates a comparison of the CV curves for materials taken from batteries with different SoH measured at $20 \mu\text{V s}^{-1}$. For the fresh electrodes, from the 100 % SoH cell, the H1-M peak was divided into two clearly distinct peaks that were related to a two-step phase transition. With the decreasing battery SoH, the peaks were merged into one peak and became wider because of the slower Li^+ diffusion. The peaks related to the M-H2 and H2-H3 phase transition lose intensity dramatically demonstrating exclusion of the M-H2 and H2-H3 phase transition from the redox processes. All these observations demonstrate the active material degradation from different aspects: (1) suffering of Li^+ diffusion originates from defects in the crystal lattice, cation mixing, CEI growth and formation of additional phases and (2) excluding the active material from redox processes comes from metal leaching, Li loss and irreversible phase transitions. Both mechanisms also support and aggravate each other. Analysis of UdCdV^{-1} curves calculated from the positive electrodes charge-discharge curves from the batteries aged to different SoH (Fig. S10, Supplementary note 1) is in agreement with the CV results.

Regarding temperature dependence (Fig. S7b), no clear effect on the electrochemical properties was observed, and the results of the rate capability and CV measurements were similar for the positive electrodes aged at 5 °C, 23 °C, and 45 °C demonstrating similar stability of the electrode material at the high range of temperatures. Broaden peaks for the electrode cycled at 23 °C at high scan rates (Fig. S8e and Fig. S9e) can be related with higher number of cycles or with experimental error.

3.3. Negative electrodes

Negative electrodes were taken from the same battery cells as the positive electrodes described in the previous section. Visually, all unfolded negative electrodes looked different from each other, and

appeared damaged. For the fresh electrodes and the electrodes from the batteries cycled down to 80 % SoH at 23 °C and 45 °C, graphite was observed on both sides of the copper foil, and for the electrodes with cycled to 30 % and 50 % SoH at 45 °C and to 80 % SoH at 5 °C, graphite was detached from the copper foil current collector and stuck to the separator which is possibly related to Li plating and Li dendrites binding the graphite to the separator.

3.3.1. Morphology

In the SEM measurements, the fresh and aged samples were compared. Magnified images of the negative electrodes were presented in Fig. 5 a-c and Fig. S11 to visualize changes in the structure induced by the difference in SoH of the batteries. All the samples seem to have a prominent secondary structure. After cycling the batteries at 45 °C the negative electrode surface had become more degraded as can be seen from the appearance of additional pores and inhomogeneities, while most of the graphite particles appeared relatively unchanged compared to the fresh electrodes. Cycling at 23 °C did not make any difference compared to cycling at 45 °C. For the samples from the 30 % SoH battery, it was observed that all surface is coated with particles. Similar particles, but in lesser extent, were found on the surface of the electrode from the battery cycled at 5 °C to 80 % SoH. We assume that those can possibly be Al oxide particles from the separator. Likewise, a visual inspection of the negative electrode confirms that the separator is stuck to the electrode material, which may indicate lithium dendrite growth attaching the electrode to the separator. The mean secondary particle size of graphite is approximately 14–18 μm as is shown in the diagrams of the particle size distribution in Fig. 5d.

Particle size was increased with the decreasing SoH, and the dependence was close to linear except for the electrode taken from the fresh battery demonstrating low degradation of the negative electrode prior to cycling. Size of the particles is similar with the one calculated for the negative electrode aged to 80 % SoH at 45 °C (Fig. S12). The sample aged at 23 °C had a similar particle size distribution as the sample aged at 45 °C to 50 % SoH which can be related to dependence of degradation on cycle number, not only the cell SoH value. Cycling at 5 °C leads to a dramatic drop in particle size distribution suggesting crack formation and pulverization of the graphite particles under these conditions. No cracks are observed on the surface of the fresh sample with low magnification, but micro-cracks can be observed for the aged samples from the 80 % and 50 % SoH batteries. For the samples from the cells aged to 30 % SoH at 45 °C, and aged to 80 % SoH at 5 °C, it is not possible to observe any cracks as the Al_2O_x particles from the separator coat the negative electrode surface of these samples. Similar to the positive electrode, the volume changes are due to lithium intercalation and deintercalation which expands and contracts the graphite interlayer distance. Furthermore, small gaps between the particles and the surrounding binder were observed, which can originate from volume changes during the delithiation/lithiation processes or from cavity formation [70] disintegrating these materials.

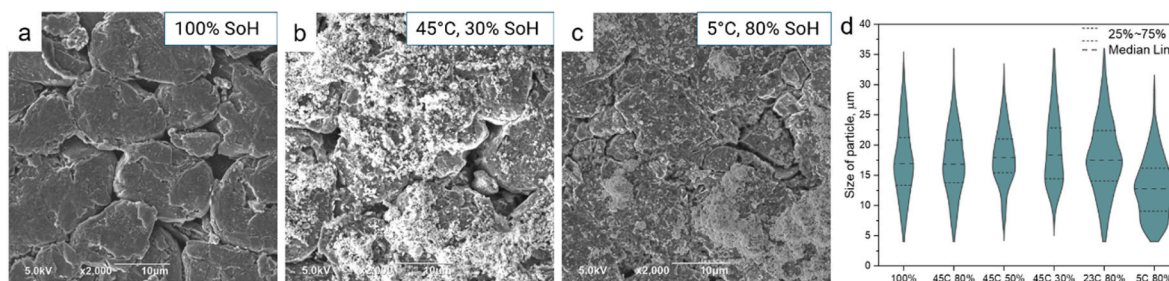


Fig. 5. The SEM images of the negative electrode samples (a) from the fresh battery and from the batteries aged at (b) 45 °C to 30 % SoH and (c) at 5 °C to 80 % SoH obtained with 2000 \times magnification. (d) Size distribution analysis of all negative electrode samples. Thickness of the cyan bars is related to number of particles of corresponding size.

3.3.2. Atomic composition

Table S4 and Fig. S13 represent the distribution of all observed elements for the aged and fresh samples based on the EDX analysis. The negative electrode materials consist mostly of elements C, O, F, Si, Al, S, and P suggesting that the main active material is graphite with added Si particles. Carbon with concentration from 37 to 89 at.% for different samples (Fig. S13) was found the main active component of the negative electrode, originating from the active material, binder, and SEI layer. Its concentration decreases with the decreasing SoH, increasing cycling number, and decreasing cycling temperature. The decrease is related to SEI growth and covering of the surface by other components during the cycling process [13]. Oxygen from oxide species with concentration from 7 to 44 at%, fluorine from the electrolyte and possibly from the binder with concentration from 2 to 12 at% and phosphorus from the electrolyte with concentration from 0.2 to 1.2 at% contribute significantly. Their concentrations generally show an opposite growth trend to the carbon concentration due to the same processes. However, the P and F concentration reached higher values for the negative electrode aged to 80 % SoH at 23 °C, which can be attributed to measurement error. Silicon with concentration from 0.7 to 1.1 at% is another active component whose concentration was increased slightly with decreasing SoH. As EDX is surface analysis, this suggests leaching of Si from the bulk and deposition in the SEI layer. It is well-known that Si species are not stable during cycling in Li batteries. However, in some cases (for example, Si nanoparticles of Si/C composites) those structures can remain relatively stable [71]. Aluminum content grows from almost 0 at % for the electrodes from the fresh cell to 4 at% for the electrodes from the 50 % and 30 % SoH batteries and even to 12 at% for the electrode aged at 5 °C.

To find where Al originates from, both sides of the separator were investigated (Fig. S14, Table S5). Separator sample from the cell aged to 80 % SoH at 5 °C was chosen because the negative electrode from this cell has the highest amount of Al. EDX analysis demonstrated significant difference in atomic composition of two separator sides. Side 1 was facing the positive electrode consists of C (86.73 at.%) and O (10.04 at. %). Traces of F, P and S can be originated from electrolyte; Zn traces can be included in the separator; Ni, Co, and Mn atoms most likely were stuck when migrating from the positive to negative side as no NMC

particles were observed on the separator surface. The SEM image of this material is typical for polymer [72]. The side facing the negative electrode consists of Al (32.36 at.%) and O (56.48 at.%) suggesting Al_2O_x particles covering the whole Side 2 as visible on the SEM image of Side 2. It is known that Al_2O_x coating can improve wettability, mechanical and thermal properties of a separator, prevent short-circuiting and thermal runaway [73]. Because Al_2O_x material covers the separator from the negative electrode side, Li dendrites are growing during long cycling or cycling at low temperatures penetrating from the graphite layer to the separator, so Al can be found on the negative electrode surface.

With decreased SoH and at low temperature, the amounts of Ni, Co, and Mn increased on the surface of the negative electrode which suggests metals liberate and migrating from the positive to the negative electrode. (Fig. 6d). While Co concentration is relatively similar (increased from 0 to 0.02 at.% without a visible trend), the amount of Ni increased from 0.01 at.% for the fresh electrode to 0.04 at.% for the sample from the 30 % SoH aged cell. It increases significantly up to 0.15 at.% for electrode aged at 5 °C. The concentration of Mn was increased also significantly (up to 0.04 at%) for the sample aged at low temperatures. It is noticeable that the amount of Mn compared to the amount of Ni ions on the negative electrode surface was much higher than it should be according to the original structure which is close to NMC811 confirming statements made in the previous chapter that Mn is the most easily leaching transition metal in the positive electrode. Increasing Mn content on negative electrode surface at 5 °C originates from excessive SEI growth occurring at low temperatures. Manganese dissolution from a positive and deposition to a negative electrode is typical for aged batteries with increasing amounts of the transferred manganese reported with increasing cycling temperature [13,48]. In general, transition metal deposition from a positive to negative electrode depends on impurities in the electrolyte (HF presence) and cycling voltage [44]. It has been reported earlier that the dissolution of nickel, manganese, or cobalt from the positive electrode is a major aging mechanism due to the loss of cyclable lithium which originates from excluding active material from Li^+ storage. Moreover, Ni, Co, and Mn deposition on the negative electrode accelerates SEI growth and can lead to its decomposition. Additionally, it has been shown that the loss of lithium is larger when

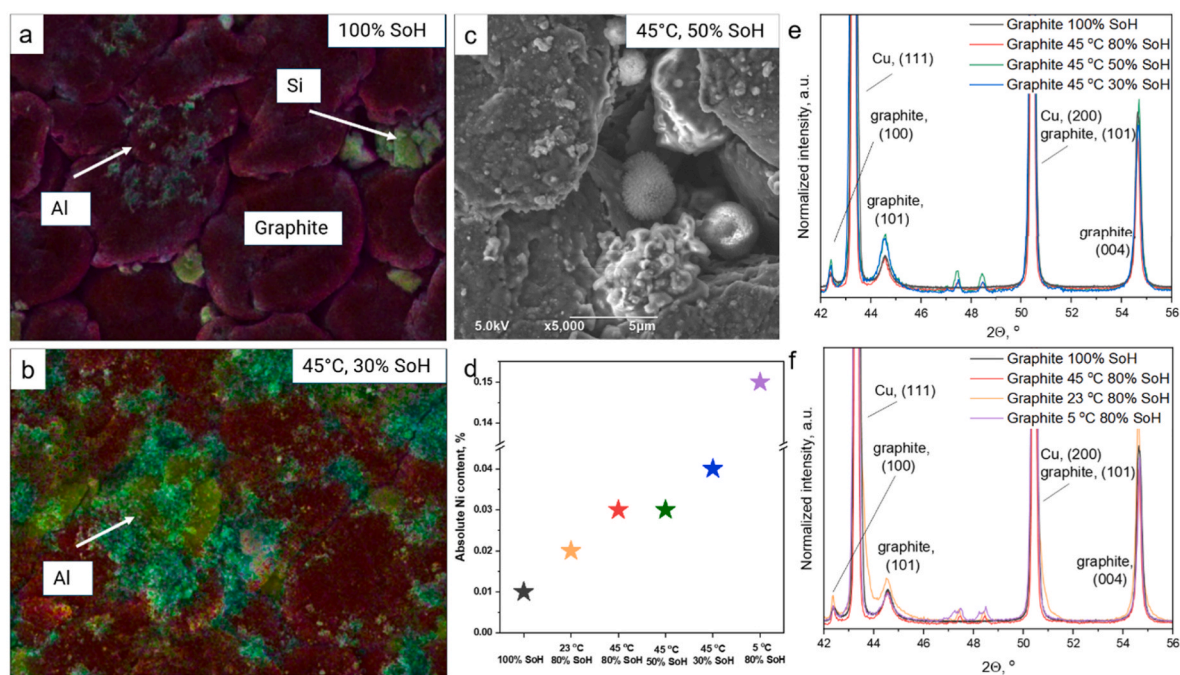


Fig. 6. An EDX layered map of negative electrode atomic compositions from the fresh batteries (a) and batteries aged to 30 % SoH at 45 °C (b). A SEM image of spherical particles found on the surface of the sample from the battery aged at 45 °C to 50 % SoH (c). Ni atomic concentration on the surface of the negative electrodes (d). Magnified diffractograms for the negative electrode from the batteries with the different SoH (e) and aged at different temperatures (f).

manganese is deposited on negative electrode compared to nickel or cobalt [46,74].

The EDX layered maps of the negative electrode elemental compositions were reconstructed from the EDX data, which was shown in Fig. 6a, b and Fig. S15. Cycling leads to the detachment of AlO_x particles originating from the separator and deposition on the negative electrode surface, and for the 30 % SoH, most of the electrode surface was covered with AlO_x particles. The Si particles became less and less visible with decreasing SoH but the EDX concentration did not change much. We correlate this is due to the decomposition of the Si particles and their inclusion into the SEI layer.

Another important feature found during the SEM observation is the formation of spherical features not detected by EDX (Fig. 6c). These features were found for a few electrodes, and their appearance were very rare. On the EDX mapping, they were not visible and merged with the carbon background. We suggest the formation of Li_2CO_3 clusters [75] or Li dendrites because Li is not detectable by the EDX.

3.3.3. Structural properties

Fig. 6e, f and Figs. S16 and S17 summarize XRD patterns normalized to (002) peak for the negative electrode samples. The main component of the negative electrodes is graphite, belongs to the $P6_3/mmc$ space group which is confirmed by the measured spectra. The XRD diffractograms show its typical (002), (004), and (110) reflections [76]. Additionally, copper reflections indicate the presence of copper in the electrode, specifically in the current collector. No additional Li_2CO_3 or LiF reflection peaks were detected between 20 and 40°. Broadening of the peak intensity was observed for the (002) and (004) reflections for the aged samples. The result might be caused by an increased disorder in the crystal structure and decreased crystal size.

A few extra phases with the peaks at 29.5°, 47.5°, 48.5°, and 77.5° were observed for the electrodes from the batteries with SoH 80 % (especially, for the one cycled at 5 °C), 50 %, and 30 % SoH but their nature was not clear. Those can be related to the formation of the SEI layer and other species formed during the cycling. The electrodes from the cells cycled down to the 50 % SoH was different from the others and

featured by higher peaks and the highest intensity of the extra phase peaks. It can be caused by inhomogeneous aging of the cells which had led to different material degradation inside the cell. This result is analogical to the observations for the NMC positive electrode from the same cell. For the negative electrodes, we observed that with decreasing in the SoH. There was a general trend of an increase of the (004) and (110) peaks normalized with respect to the peak (002) as well as their broadening which may be related to graphite exfoliation and crystal disordering [77]. Traces of the Si-related peaks (the *Cmca* space group) also was found but their intensity was comparatively low. This, however, confirmed the observation of Si in the EDX results.

3.3.4. Electrochemical properties

Results of the rate capability measurements were shown in Fig. 7a and b. For non-cycled batteries, the low C rate cycle is important for CEI/SEI formation and here 0.03 C is a conditioning cycle. In our case, all the batteries were formatted, however, to follow typical cycling protocol and to form CEI/SEI layers in the case of any damages formed during the opening and assembling the testing cells, conditioning cycles were applied. The capacity at this C-rate ($\sim 425 \text{ mA h g}^{-1}$) was higher compared with the one expected for graphite (375 mA h g^{-1}) due to the presence of the Si particles which have a theoretical capacity near 3579 mA h g^{-1} [71]. However, with the decreasing battery SoH the extracted negative electrode capacity drops down to $300\text{--}350 \text{ mA h g}^{-1}$, and those values were slightly different for the investigated samples. The sample aged at 5 °C shows especially poor capacity near 150 mA h g^{-1} at 0.03 C which indicates the dramatic capacity loss of the negative electrode at the low operating temperature. The rate capability measurements showed that the capacity fade was reduced to some extent if the charging and discharging is done with 2 C or above. The coulombic efficiency of the fresh and the aged electrodes remains close to 100 % for all the C-rates. However, at the higher C-rates the capacity fade was faster and the coulombic efficiency lower. In general, the negative electrodes showed a good rate capability performance despite of the aging.

The capacity at 0.1 C of the negative electrodes decreased from 319

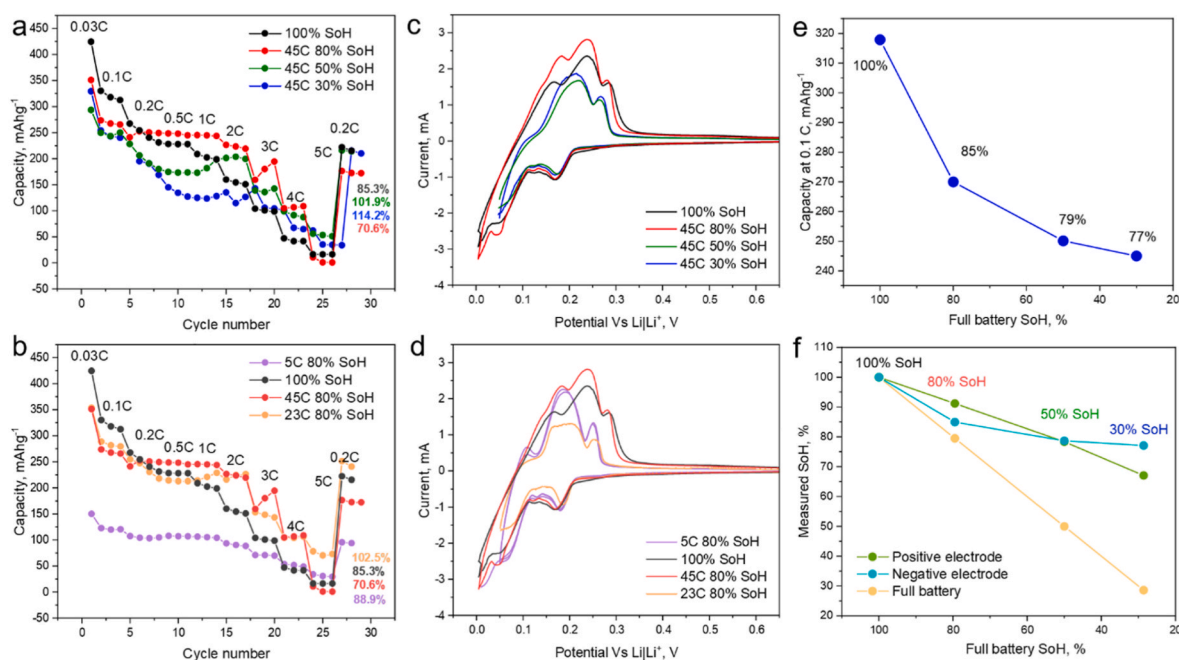
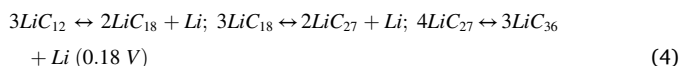


Fig. 7. Rate capability measurements for the negative electrodes (a) aged to the different SoH levels (b) and aged at different temperatures. CV curves of the negative electrodes ($20 \mu\text{V s}^{-1}$ scan rate in 3-electrode cell vs $\text{Li}|\text{Li}^+$) from the batteries (c) aged to the different SoH levels and (d) aged at different temperatures. (e) The 0.1 C-rate capacity of the negative electrode materials from the cells aged to the different SoH levels. (f) Comparison of the capacity of the full batteries, positive and negative electrodes at different SoH.

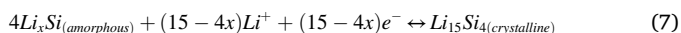
mA h g⁻¹ to 245 mA h g⁻¹ (77 % of the original capacity) when the battery SoH decreased from 100 % to 30 % as shown in Fig. 7e. At 1 C, the capacity at first increases from 205 mA h g⁻¹ to 245 mA h g⁻¹ and then decreased to 120 mA h g⁻¹ with the decreasing battery SoH (Fig. S18). At the low C-rates, the capacity is limited by the amount of the electrode active materials participating in the redox processes. The capacity fade implies the degradation of the active materials accompanied by graphite exfoliation, Si liberation, SEI growth and decomposition, and negative electrode contamination. At the high C-rates, Li-ion mass transfer and the amount of the active materials define the capacity. Guo et al. suggested extension of interlayer space in graphite which allow more Li-ions to be intercalated [78]. Tortuosity changes can be the other reason of capacity increase with first circles.

As for temperature dependency, capacity and rate capability of the samples cycled at 23 °C and 45 °C showed similar trend as described above. The electrodes aged at 5 °C have much lower capacity compared with the fresh ones and those aged at the other temperatures, indicating significant changes in the electrode material structure which is in the agreement with the XRD and SEM data (Fig. 6) showing damaged particles and crystals.

CV curves of the fresh and aged electrode sample in Fig. 7c,d, Fig. S19, and Fig. S20 showed all three-phase transition peaks typical for graphite with 20, 50, and 100 μV s⁻¹ scan rates. Levi et al. reported that these three peaks correspond to the following electrochemical phase transitions of graphite according to Equations (3)–(5) [79]:



Peaks at 0.17 V, 0.33 V and 0.51 V on the charge curve and 0.2 C on the discharge curve are expected to appear to indicate presence of Si according to Equations (6) and (7) [80,81]:



The CV curves measured for all samples demonstrated the presence of all the described graphite – Li intercalation peaks at 100 μV s⁻¹, 50 μV s⁻¹, and 20 μV s⁻¹. Reducing the battery SoH to 50 % significantly decreased the height of the first and second graphite phase transition peaks (Equations (3) and (4)), especially at 100 μV s⁻¹. Further increasing of SoH to 30 % made the reduction of the peak even more significant. A decrease in the battery SoH led to a shift of the peaks on the charge curve to the lower potentials and the peaks on the discharge curve to the higher potentials, and this effect was more pronounced for the low scan rates than for the high ones. The peaks on the CV curve became narrower as the SoH level decreased, indicating a better diffusion of Li-ions through graphite crystal with decreasing SoH [69]. It may happen because some active material is expanded providing better Li⁺ pathways [78] and resulting in activation as diffusion is facilitated. For the fresh samples, the peaks of the first phase transition (Equation (3)) were more discerned than those for the aged samples which can be related with higher efficiency of the final step of lithiation for the fresh electrode comparing to the aged ones. Analysis of dCdV⁻¹ curves calculated from the charge-discharge curves of the negative electrodes from the batteries aged to different SoH (Fig. S22, Supplementary note 2) were in agreement with CV results. Peaks representing reactions involved Si at 0.17 V and 0.33 V were merged with graphite induced peaks, and hence any effect of Si cannot be recognized. However, a peak near 0.5 V can be clearly observed (Fig. S21a). Intensity of this peak decreased significantly with decreasing SoH suggesting Si liberation as demonstrated by the EDX analysis (Fig. 6).

It is important to note that the sample aged at 5 °C had all the peaks related to the phase transition while the peaks of the sample aged at 23 °C were merged. In first thought, this is surprising as the samples behaved in an opposite manner in the rate capability tests. However, the CV curves reflect electrochemical processes, and their rate remains unchanged after the low temperature cycling whereas the long cycling at 23 °C leads to suppressing of the phase transitions. Hence, the capacity loss of negative electrode at the low temperatures originates from the structural damage confirmed by the SEM and XRD results, but not from the electrochemical reactions becoming more sluggish. Fig. S21b represents behavior of the peak near 0.5V related to interaction of Si with Li⁺. For the fresh samples and the sample aged at 23 °C, this peak showed similar intensity. Increasing aging temperature to 45 °C leads to the peak decrease whereas after 5 °C aging, the peak almost disappears. With the low Si concentration and low number of experimental points, it was hard to observe any trend in Si behavior, though low and high temperature appear to improve Si liberation.

4. Conclusions

In this work, the mechanisms of aging of NMC positive electrode and Si-Graphite negative electrode materials harvested from commercial 18,650 cylindrical format cells were investigated. Aged electrode samples were characterized using structural and electrochemical methods and compared with fresh samples. Based on the characterization results of the commercial NMC811/Si-Graphite batteries cycled at 5 °C, 23 °C and 45 °C to different SoH, several aging mechanisms had been found and summarized in Table 1. Microcracking, particle cracks and exfoliation of the active materials in both the aged positive electrodes and negative electrodes are suggesting that the active materials experienced loss of electrical and mechanical contact between the particles, trap Li-ions between electrode material agglomerates, thus causing impedance growth and capacity fade. Additionally, we found particles deposited on the negative electrodes after the aging and these can be Li dendrites or Li carbonate agglomerates. SEI layer has tendency to growth with decreasing SoH. Transition metals were dissolved from the positive electrode and were depositing on the negative electrode with a decreasing on the host battery SoH. Si had also tended to liberate, but it remained in the electrolyte and SEI layer. Li/transition metals mixing was found to increase with decrease SoH. Electrode degradation leads to capacity drop of active materials because of diffusion limitations, leaching of active materials, cation mixing, disordering, and resulting in decreasing capacity of electrodes and diminishing of the phase transformations.

Graphite was observed to sustain aging at 45 °C moderately even though microcracks were observed and lithium plating was suspected. The positive electrode NMC811 was facing a severe amount of microcracking, particle exfoliation, cation mixing, CEI growth, transition metal leaching, Li diffusion limitations, and extra phase formation. The negative electrodes suffered from microcracking, particle exfoliation, SEI growth, transition metal contamination, extra phase formation, and Li plating. All these effects led to capacity fade and diffusion difficulties facing loss of the full battery cell.

Both positive and negative electrode materials were degraded slower than the whole Li-ion battery (Fig. 7f), and the negative electrode suffered less than the positive electrode from the capacity fade. The positive electrode degradation limited the performance of the NMC811/graphite battery at 45 °C when negative electrode degradation mainly leads to capacity fade at 5 °C.

Funding

Ekaterina Laakso reports financial support was provided by Horizon 2020 European Innovation Council Fast Track to Innovation. Sofya Efimova reports financial support was provided by Horizon 2020 European Innovation Council Fast Track to Innovation. Pertti Kauranen

Table 1
Summary of LiB aging mechanisms discussed in the manuscript.

#	Method	Observation	Result
1	SEM: low magnification	Microcracking in the aged positive electrodes and negative electrodes with decreasing SoH	Loss of electrical contacts → resistance increase
2	SEM: high magnification	Increasing particle size of the positive and negative electrodes with decreasing SoH	Exfoliating processes → crystal cracks, Li trap, resistance increase
3	SEM: high magnification	Reducing the particle size of the negative electrode particles at low temperature	Particle cracking → loss of electrical contacts and resistance increase
4	SEM, EDX	Agglomerates deposited on the negative electrodes after the aging which can be Li dendrites or Li carbonate agglomerates	Li loss, short circuit, thermal runaway
5	EDX	Slight increase in concentration of the electrolyte elements on the surface of the aged negative electrodes	SEI growth → electrolyte loss and surface resistance increase
6	EDX, NEXAFS	Transition metals dissolution from the positive electrode and its deposition on the negative electrode with decreasing the battery SoH. Ni and Mn are the most active transition metals in this process.	Active material removal, negative electrode contamination → capacity drop, resistance increase
7	EDX, CV	Si dissolution on negative electrode with decreasing SoH. Si remains in the electrolyte and SEI layer	Active material removal, electrolyte/SEI contamination → capacity drop, resistance increase
8	XRD	Exfoliation and decreasing crystal size of positive and negative electrode particles	Reducing electrical and mechanical contact between the particles, trap Li-ions between electrode material agglomerates → impedance growth and capacity fade
9	XANES, XRD	Li/transition metals mixing with decrease SoH	Li loss, active material degradation → impedance growth and capacity fade
10	Rate capability tests	Capacity of positive and negative electrodes decreased with the decreasing SoH at low C-rates	Degradation of active materials → impedance growth and capacity fade
11	Rate capability tests	Capacity increase at the high C-rates from 100 % SoH to 80 % SoH	Improvement of the Li-ion diffusion
12	Rate capability tests	The negative electrode aged at 5 °C showed significant capacity loss while good phase transition was still seen in the CV curves.	high level of structural damage during the low temperature cycling which did not affect the electrochemical phase transitions
13	CV	Diminishing of the H2 – H3 phase transformation occurring in the aged positive electrode materials	Capacity fade due to Li ⁺ bulk diffusion limitations
14	CV	Flattening and disappearance of all the peaks for the positive electrode materials	Disordering and elements liberation

reports financial support was provided by Horizon 2020 European Innovation Council Fast Track to Innovation. Katja Lahtinen reports financial support was provided by Horizon 2020 European Innovation Council Fast Track to Innovation. Emilio Napolitano reports financial support was provided by Horizon 2020 European Innovation Council

Fast Track to Innovation. Vanesa Ruiz reports financial support was provided by Horizon 2020 European Innovation Council Fast Track to Innovation. Joze Moskon reports financial support was provided by Horizon 2020 European Innovation Council Fast Track to Innovation. Miran Gaberscek reports was provided by Horizon 2020 European Innovation Council Fast Track to Innovation. Juyeon Park reports was provided by Horizon 2020 European Innovation Council Fast Track to Innovation. Steffen Seitz reports financial support was provided by Horizon 2020 European Innovation Council Fast Track to Innovation. Tanja Kallio reports financial support was provided by Horizon 2020 European Innovation Council Fast Track to Innovation. The work is done using the Aalto University Otanano and RAMI infrastructures.

CRedit authorship contribution statement

Ekaterina Laakso: Formal analysis, Investigation, Writing – original draft. **Sofya Efimova:** Investigation, Writing – original draft. **Mattia Colalongo:** Investigation. **Pertti Kauranen:** Investigation, Writing – review & editing. **Katja Lahtinen:** Investigation, Writing – review & editing. **Emilio Napolitano:** Investigation, Writing – review & editing. **Vanesa Ruiz:** Investigation, Writing – review & editing. **Jozé Moskon:** Investigation. **Miran Gabersček:** Investigation. **Juyeon Park:** Investigation, Writing – review & editing. **Steffen Seitz:** Project administration, Supervision, Writing – review & editing. **Tanja Kallio:** Resources, Supervision, Writing – review & editing.

Declaration of competing interest

The authors declare that they have no conflict of interest.

Data availability

Data will be made available on request.

Acknowledgment

This project (17IND10-LiBforSecUse) has received funding from the EMPIR programme co-financed by the Participating States and from the European Union's Horizon 2020 research and innovation programme.

Appendix A. Supplementary data

Supplementary data to this article can be found online at <https://doi.org/10.1016/j.jpowsour.2024.234159>.

References

- [1] A. Yoshino, The birth of the lithium-ion battery, *Angew. Chem. Int. Ed.* 51 (2012) 5798–5800, <https://doi.org/10.1002/anie.201105006>.
- [2] T. Nakajima, Akira, Kenichi Yoshino, Sanechika, *Secondary Battery, US4668595A*, 1887.
- [3] D. Deng, Li-ion batteries: Basics, progress, and challenges, *Energy Sci. Eng.* 3 (2015) 385–418, <https://doi.org/10.1002/ese3.95>.
- [4] T. Sasaki, Y. Ukyo, P. Novák, Memory effect in a lithium-ion battery, *Nat. Mater.* 12 (2013) 569–575, <https://doi.org/10.1038/nmat3623>.
- [5] L. Kong, C. Li, J. Jiang, M.G. Pecht, Li-ion battery fire hazards and safety strategies, *Energies* 11 (2018) 1–11, <https://doi.org/10.3390/en11092191>.
- [6] B. Scrosati, J. Garche, Lithium batteries: status, prospects and future, *J. Power Sources* 195 (2010) 2419–2430, <https://doi.org/10.1016/j.jpowsour.2009.11.048>.
- [7] Y. Cui, C. Du, G. Yin, Y. Gao, L. Zhang, T. Guan, L. Yang, F. Wang, Multi-stress Factor Model for Cycle Lifetime Prediction of Lithium Ion Batteries with Shallow-Depth Discharge, Elsevier Ltd, 2015, <https://doi.org/10.1016/j.jpowsour.2015.01.003>.
- [8] S. Saxena, C. Hendricks, M. Pecht, Cycle life testing and modeling of graphite/LiCoO₂ cells under different state of charge ranges, *J. Power Sources* 327 (2016) 394–400, <https://doi.org/10.1016/j.jpowsour.2016.07.057>.
- [9] A. Krupp, R. Beckmann, T. Diekmann, E. Ferg, F. Scholdt, C. Agert, Calendar aging model for lithium-ion batteries considering the influence of cell characterization, *J. Energy Storage* 45 (2022) 103506, <https://doi.org/10.1016/j.est.2021.103506>.
- [10] M. Maures, Y. Zhang, C. Martin, J.Y. Delétage, J.M. Vlassa, O. Briat, Impact of temperature on calendar ageing of Lithium-ion battery using incremental capacity

- analysis, *Microelectron. Reliab.* 100–101 (2019) 113364, <https://doi.org/10.1016/j.microrel.2019.06.056>.
- [11] D. Capkova, V. Knap, A.S. Fedorkova, D.I. Stroe, Investigation of the temperature and DOD effect on the performance-degradation behavior of lithium-sulfur pouch cells during calendar aging, *Appl. Energy* 332 (2023) 120543, <https://doi.org/10.1016/j.apenergy.2022.120543>.
- [12] R. Jung, R. Morasch, P. Karayaylali, K. Phillips, F. Maglia, C. Stinner, Y. Shao-Horn, H.A. Gasteiger, Effect of ambient storage on the degradation of Ni-rich positive electrode materials (NMC811) for Li-ion batteries, *J. Electrochem. Soc.* 165 (2018) A132–A141, <https://doi.org/10.1149/2.0401802jes>.
- [13] T. Waldmann, M. Wilka, M. Kasper, M. Fleischhammer, M. Wohlfahrt-Mehrens, Temperature dependent ageing mechanisms in Lithium-ion batteries – a Post-Mortem study, *J. Power Sources* 262 (2014) 129–135, <https://doi.org/10.1016/j.jpowsour.2014.03.112>.
- [14] R. Kantharaj, A.M. Marconnet, Heat generation and thermal transport in lithium-ion batteries: a scale-bridging perspective, *Nanoscale Microscale Thermophys. Eng.* 23 (2019) 128–156, <https://doi.org/10.1080/15567265.2019.1572679>.
- [15] R. Genieser, S. Ferrari, M. Loveridge, S.D. Beattie, R. Beanland, H. Amari, G. West, R. Bhagat, Lithium ion batteries (NMC/graphite) cycling at 80 °C: different electrolytes and related degradation mechanism, *J. Power Sources* 373 (2018) 172–183, <https://doi.org/10.1016/j.jpowsour.2017.11.014>.
- [16] J. Guo, S. Jin, X. Sui, X. Huang, Y. Xu, Y. Li, P.K. Kristensen, D. Wang, K. Pedersen, L. Gurevich, D.I. Stroe, Unravelling and quantifying the aging processes of commercial Li(Ni_{0.5}Co_{0.2}Mn_{0.3})O₂/graphite lithium-ion batteries under constant current cycling, *J. Mater. Chem. A* 11 (2022) 41–52, <https://doi.org/10.1039/d2ta05960f>.
- [17] J. Henschel, F. Horsthemke, Y.P. Stenzel, M. Evertz, S. Girod, C. Lürenbaum, K. Kösters, S. Wiemers-Meyer, M. Winter, S. Nowak, Lithium ion battery electrolyte degradation of field-tested electric vehicle battery cells – a comprehensive analytical study, *J. Power Sources* 447 (2020), <https://doi.org/10.1016/j.jpowsour.2019.227370>.
- [18] P.M. Attia, A. Bills, F. Brosa Planella, P. Dechent, G. dos Reis, M. Dubarry, P. Gasper, R. Gilchrist, S. Greenbank, D. Howey, O. Liu, E. Khoo, Y. Preger, A. Soni, S. Sripad, A.G. Stefanopoulou, V. Sulzer, Review—“Knees” in lithium-ion battery aging trajectories, *J. Electrochem. Soc.* 169 (2022) 060517, <https://doi.org/10.1149/1945-7111/ac6d13>.
- [19] V.A. Agubra, J.W. Fergus, The formation and stability of the solid electrolyte interface on the graphite anode, *J. Power Sources* 268 (2014) 153–162, <https://doi.org/10.1016/j.jpowsour.2014.06.024>.
- [20] S.K. Heiskanen, J. Kim, B.L. Lucht, Generation and evolution of the solid electrolyte interphase of lithium-ion batteries, *Joule* 3 (2019) 2322–2333, <https://doi.org/10.1016/j.joule.2019.08.018>.
- [21] C. Hendricks, N. Williard, S. Mathew, M. Pecht, A failure modes, mechanisms, and effects analysis (FMMEA) of lithium-ion batteries, *J. Power Sources* 297 (2015) 113–120, <https://doi.org/10.1016/j.jpowsour.2015.07.100>.
- [22] B. Xu, A. Oudalov, A. Ulbig, G. Andersson, D.S. Kirschen, Modeling of lithium-ion battery degradation for cell life assessment, *IEEE Trans. Smart Grid* 9 (2018) 1131–1140, <https://doi.org/10.1109/TSG.2016.2578950>.
- [23] P. Teichert, H. Jahnke, E. Figgemeier, Degradation mechanism of monocrystalline Ni-rich Li[Ni_xMn_yCo_z]O₂ (NMC) active material in lithium ion batteries, *J. Electrochem. Soc.* 168 (2021) 090532, <https://doi.org/10.1149/1945-7111/ac239f>.
- [24] A. Kushima, K.P. So, C. Su, P. Bai, N. Kuriyama, T. Maebashi, Y. Fujiwara, M. Z. Bazant, J. Li, Liquid cell transmission electron microscopy observation of lithium metal growth and dissolution: root growth, dead lithium and lithium flotsams, *Nano Energy* 32 (2017) 271–279, <https://doi.org/10.1016/j.nanoen.2016.12.001>.
- [25] R. Khurana, J.L. Schaefer, L.A. Archer, G.W. Coates, Suppression of lithium dendrite growth using cross-linked polyethylene/poly(ethylene oxide) electrolytes: a new approach for practical lithium-metal polymer batteries, *J. Am. Chem. Soc.* 136 (2014) 7395–7402, <https://doi.org/10.1021/ja502133j>.
- [26] X. Lin, K. Khosravinia, X. Hu, J. Li, W. Lu, Lithium plating mechanism, detection, and mitigation in lithium-ion batteries, *Prog. Energy Combust. Sci.* 87 (2021) 100953, <https://doi.org/10.1016/j.pecs.2021.100953>.
- [27] Z. Ahaliabadeh, X. Kong, E. Fedorovskaya, T. Kallio, Extensive comparison of doping and coating strategies for Ni-rich positive electrode materials, *J. Power Sources* 540 (2022) 231633, <https://doi.org/10.1016/j.jpowsour.2022.231633>.
- [28] S. Hwang, S.M. Kim, S.M. Bak, K.Y. Chung, W. Chang, Investigating the reversibility of structural modifications of Li_xNi_yMn_zCo_{1-y-z}O₂ cathode materials during initial charge/discharge, at multiple length scales, *Chem. Mater.* 27 (2015) 6044–6052, <https://doi.org/10.1021/acs.chemmater.5b02457>.
- [29] X. Kong, D. Li, E.O. Fedorovskaya, T. Kallio, X. Ren, New insights in Al-doping effects on the LiNiO₂ positive electrode material by a sol-gel method, *Int. J. Energy Res.* 45 (2021) 10489–10499, <https://doi.org/10.1002/er.6536>.
- [30] T. Li, X.-Z. Yuan, L. Zhang, D. Song, K. Shi, C. Bock, Degradation mechanisms and mitigation strategies of nickel-rich NMC-based lithium-ion batteries, *Electrochem. Energy Rev.* 3 (2020) 43–80, <https://doi.org/10.1007/s41918-019-00053-3>.
- [31] B.L.D. Rinkel, J.P. Vivek, N. Garcia-Araez, C.P. Grey, Two electrolyte decomposition pathways at nickel-rich cathode surfaces in lithium-ion batteries, *Energy Environ. Sci.* 15 (2022) 3416–3438, <https://doi.org/10.1039/d1ee04053g>.
- [32] S. Muto, Y. Sasano, K. Tatsumi, T. Sasaki, K. Horibuchi, Y. Takeuchi, Y. Ukyo, Capacity-fading mechanisms of LiNiO₂[sub 2]-based lithium-ion batteries, *J. Electrochem. Soc.* 156 (2009) A371, <https://doi.org/10.1149/1.3076137>.
- [33] D. Abraham, R. Twisten, M. Balasubramanian, I. Petrov, J. McBreen, K. Amine, Surface changes on LiNi_{0.8}Co_{0.2}O₂ particles during testing of high-power lithium-ion cells, *Electrochem. Commun.* 4 (2002) 620–625, [https://doi.org/10.1016/S1388-2481\(02\)00388-0](https://doi.org/10.1016/S1388-2481(02)00388-0).
- [34] Y. Domi, T. Doi, M. Ochida, T. Yamanaka, T. Abe, Z. Ogumi, Intercalation/de-intercalation reactions of lithium ion at graphite in electrolyte solutions containing 3D-transition-metal ions and cyclic ethers, *J. Electrochem. Soc.* 163 (2016) A2849–A2853, <https://doi.org/10.1149/2.0111614jes>.
- [35] E. Peled, S. Menkin, Review—SEI: past, present and future, *J. Electrochem. Soc.* 164 (2017) A1703–A1719, <https://doi.org/10.1149/2.1441707jes>.
- [36] S.P. Kühn, K. Edström, M. Winter, I. Cekic-Laskovic, Face to face at the cathode electrolyte interphase: from interface features to interphase formation and dynamics, *Adv. Mater. Interfaces* 9 (2022), <https://doi.org/10.1002/admi.202102078>.
- [37] Z. Zhang, J. Yang, W. Huang, H. Wang, W. Zhou, Y. Li, Y. Li, J. Xu, W. Huang, W. Chiu, Y. Cui, Cathode-electrolyte interphase in lithium batteries revealed by cryogenic electron microscopy, *Matter* 4 (2021) 302–312, <https://doi.org/10.1016/j.matt.2020.10.021>.
- [38] L.S. Kremer, T. Danner, S. Hein, A. Hoffmann, B. Prifling, V. Schmidt, A. Latz, M. Wohlfahrt-Mehrens, Influence of the electrolyte salt concentration on the rate capability of ultra-thick NCM 622 electrodes, *Batter. Supercaps.* 3 (2020) 1172–1182, <https://doi.org/10.1002/batt.202000098>.
- [39] H.S. Chan, E.J.F. Dickinson, T.P. Heins, J. Park, M. Gaberšček, Y.Y. Lee, M. Heinrich, V. Ruiz, E. Napolitano, P. Kauranen, E. Fedorovskaya, J. Moškon, T. Kallio, S. Mousaviahseini, U. Krewer, G. Hinds, S. Seitz, Comparison of methodologies to estimate state-of-health of commercial Li-ion cells from electrochemical frequency response data, *J. Power Sources* 542 (2022), <https://doi.org/10.1016/j.jpowsour.2022.231814>.
- [40] C.A. Schneider, W.S. Rasband, K.W. Elieciri, HISTORICAL commentary NIH Image to ImageJ : 25 years of image analysis, *Nat. Methods* 9 (2012) 671–675, <https://doi.org/10.1038/nmeth.2089>.
- [41] K. Klementiev, K. Norén, S. Carlson, K.G.V. Sigfridsson Clauss, I. Persson, The BALDER beamline at the MAX IV laboratory, *J. Phys. Conf. Ser.* 712 (2016) 8–12, <https://doi.org/10.1088/1742-6596/712/1/012023>.
- [42] B. Ravel, M. Newville, ATHENA, artemis, hephaestus: data analysis for X-ray absorption spectroscopy using IFFFIT, *J. Synchrotron Radiat.* 12 (2005) 537–541, <https://doi.org/10.1107/S0909049505012719>.
- [43] W. Waag, S. Käbitz, D.U. Sauer, Experimental investigation of the lithium-ion battery impedance characteristic at various conditions and aging states and its influence on the application, *Appl. Energy* 102 (2013) 885–897, <https://doi.org/10.1016/j.apenergy.2012.09.030>.
- [44] K. Jalkanen, J. Karppinen, L. Skogström, T. Laurila, M. Nisula, K. Vuorilehto, Cycle aging of commercial NMC/graphite pouch cells at different temperatures, *Appl. Energy* 154 (2015) 160–172, <https://doi.org/10.1016/j.apenergy.2015.04.110>.
- [45] T. Rauhala, K. Jalkanen, T. Romann, E. Lust, N. Omar, T. Kallio, Low-temperature aging mechanisms of commercial graphite/LiFePO₄ cells cycled with a simulated electric vehicle load profile — a post-mortem study, *J. Energy Storage* 20 (2018) 344–356, <https://doi.org/10.1016/j.est.2018.10.007>.
- [46] R. Jung, F. Linsenmann, R. Thomas, J. Wandt, S. Solchenbach, F. Maglia, C. Stinner, M. Tromp, H.A. Gasteiger, Nickel, manganese, and cobalt dissolution from Ni-rich NMC and their effects on nmc622-graphite cells, *J. Electrochem. Soc.* 166 (2019) A378–A389, <https://doi.org/10.1149/2.1151902jes>.
- [47] M.M. Kabir, D.E. Demirocak, Degradation mechanism in Li-Ion Batteries : a State-Of-The-Art Review, 2017, pp. 1963–1986, <https://doi.org/10.1002/er>.
- [48] J. Vetter, P. Novák, M.R. Wagner, C. Veit, K.-C. Möller, J.O. Besenhard, M. Winter, M. Wohlfahrt-Mehrens, C. Vogler, A. Hammouche, Ageing mechanisms in lithium-ion batteries, *J. Power Sources* 147 (2005) 269–281, <https://doi.org/10.1016/j.jpowsour.2005.01.006>.
- [49] M. Kassem, C. Delacourt, Postmortem analysis of calendar-aged graphite/LiFePO₄ cells, *J. Power Sources* 235 (2013) 159–171, <https://doi.org/10.1016/j.jpowsour.2013.01.147>.
- [50] D. Yoo, Q. Liu, O. Cohen, M. Kim, K.A. Persson, Z. Zhang, Understanding the role of SEI layer in low-temperature performance of lithium-ion batteries, *ACS Appl. Mater. Interfaces* 14 (2022) 11910–11918, <https://doi.org/10.1021/acsami.1c23934>.
- [51] V. Pimenta, M. Sathiya, D. Batuk, A.M. Abakumov, D. Giaume, S. Cassaignon, D. Larher, J.-M. Tarascon, Synthesis of Li-rich NMC: a comprehensive study, *Chem. Mater.* 29 (2017) 9923–9936, <https://doi.org/10.1021/acs.chemmater.7b03230>.
- [52] A.M. Haregewoin, A.S. Wotango, B.J. Hwang, Electrolyte additives for lithium ion battery electrodes: progress and perspectives, *Energy Environ. Sci.* 9 (2016) 1955–1988, <https://doi.org/10.1039/c6ee00123h>.
- [53] T. Wang, K. Ren, W. Xiao, W. Dong, H. Qiao, A. Duan, H. Pan, Y. Yang, H. Wang, Tuning the li/ni disorder of the nmc811 cathode by thermally driven competition between lattice ordering and structure decomposition, *J. Phys. Chem. C* 124 (2020) 5600–5607, <https://doi.org/10.1021/acs.jpcc.0c00720>.
- [54] S.K. Jung, H. Gwon, J. Hong, K.Y. Park, D.H. Seo, H. Kim, J. Hyun, W. Yang, K. Kang, Understanding the degradation mechanisms of LiNi_{0.5}Co_{0.2}Mn_{0.3}O₂ cathode material in lithium ion batteries, *Adv. Energy Mater.* 4 (2014) 1–7, <https://doi.org/10.1002/aenm.201300787>.
- [55] S. Wu, X. Zhang, S. Ma, E. Fan, J. Lin, R. Chen, F. Wu, L. Li, A new insight into the capacity decay mechanism of Ni-rich layered oxide cathode for lithium-ion batteries, *Small* 18 (2022) 1–9, <https://doi.org/10.1002/sml.202204613>.
- [56] W. El Mofid, S. Ivanov, A. Bund, Effect of synthesis conditions and composition modification on the structural and electrochemical properties of layered transition metal oxide cathode materials, in: 2014 Int. Renew. Sustain. Energy Conf., IEEE, 2014, pp. 626–630, <https://doi.org/10.1109/IRSEC.2014.7059798>.
- [57] T. Pan, J. Alvarado, J. Zhu, Y. Yue, H.L. Xin, D. Nordlund, F. Lin, M.M. Doeff, Structural degradation of layered cathode materials in lithium-ion batteries

- induced by ball milling, *J. Electrochem. Soc.* 166 (2019) A1964–A1971, <https://doi.org/10.1149/2.0091910jes>.
- [58] S.H. Yu, T. Yoon, J. Mun, S. Park, Y.S. Kang, J.H. Park, S.M. Oh, Y.E. Sung, Continuous activation of Li_2MnO_3 component upon cycling in $\text{Li}_1.167\text{Ni}_0.233\text{Co}_0.100\text{Mn}_0.467\text{Mo}_0.033\text{O}_2$ cathode material for lithium ion batteries, *J. Mater. Chem. A* 1 (2013) 2833–2839, <https://doi.org/10.1039/c2ta00309k>.
- [59] D. Wang, Q. Yan, M. Li, H. Gao, J. Tian, Z. Shan, N. Wang, J. Luo, M. Zhou, Z. Chen, Boosting the cycling stability of Ni-rich layered oxide cathode by dry coating of ultrastable $\text{Li}_3\text{V}_2(\text{PO}_4)_3$ nanoparticles, *Nanoscale* 13 (2021) 2811–2819, <https://doi.org/10.1039/d0nr08305d>.
- [60] J. Li, G. Liang, W. Zheng, S. Zhang, K. Davey, W.K. Pang, Z. Guo, Addressing cation mixing in layered structured cathodes for lithium-ion batteries: a critical review, *Nano Mater. Sci.* (2022), <https://doi.org/10.1016/j.nanoms.2022.09.001>.
- [61] W. Li, Y. Jie, Y. Chen, M. Yang, Y. Chen, X. Li, Y. Guo, X. Meng, R. Cao, S. Jiao, Crossover effects of transition metal ions in high-voltage lithium metal batteries, *Nano Res.* 16 (2023) 8417–8424, <https://doi.org/10.1007/s12274-022-5334-y>.
- [62] X. Zhang, Z. Cui, A. Manthiram, Insights into the crossover effects in cells with high-nickel layered oxide cathodes and silicon/graphite composite anodes, *Adv. Energy Mater.* 12 (2022) 1–9, <https://doi.org/10.1002/aenm.202103611>.
- [63] T. Osawa, Quantitative estimation methods for concentrations and layer thicknesses of elements using edge-jump ratios of X-ray absorption spectra, *Anal. Sci.* 26 (2010) 281–284, <https://doi.org/10.2116/analsci.26.281>.
- [64] C. Heubner, M. Schneider, A. Michaelis, Diffusion-limited C-rate: a fundamental principle quantifying the intrinsic limits of Li-ion batteries, *Adv. Energy Mater.* 10 (2020), <https://doi.org/10.1002/aenm.201902523>.
- [65] P. Daubinger, M. Schelter, R. Petersohn, F. Nagler, S. Hartmann, M. Herrmann, G. A. Giffin, Impact of bracing on large format prismatic lithium-ion battery cells during aging, *Adv. Energy Mater.* 12 (2022) 2102448, <https://doi.org/10.1002/aenm.202102448>.
- [66] X. Fan, X. Ou, W. Zhao, Y. Liu, B. Zhang, J. Zhang, L. Zou, L. Seidl, Y. Li, G. Hu, C. Battaglia, Y. Yang, In situ inorganic conductive network formation in high-voltage single-crystal Ni-rich cathodes, *Nat. Commun.* 12 (2021) 1–13, <https://doi.org/10.1038/s41467-021-25611-6>.
- [67] X. Zhang, H. Jia, L. Zou, Y. Xu, L. Mu, Z. Yang, M.H. Engelhard, J.M. Kim, J. Hu, B. E. Matthews, C. Niu, C. Wang, H. Xin, F. Lin, W. Xu, Electrolyte regulating toward stabilization of cobalt-free ultrahigh-nickel layered oxide cathode in lithium-ion batteries, *ACS Energy Lett.* 6 (2021) 1324–1332, <https://doi.org/10.1021/acsenergylett.1c00374>.
- [68] C. Xu, P.J. Reeves, Q. Jacquet, C.P. Grey, Phase behavior during electrochemical cycling of Ni-rich cathode materials for Li-ion batteries, *Adv. Energy Mater.* 11 (2021) 1–29, <https://doi.org/10.1002/aenm.202003404>.
- [69] T. Kim, W. Choi, H.-C. Shin, J.-Y. Choi, J.M. Kim, M.-S. Park, W.-S. Yoon, Applications of voltammetry in lithium ion battery research, *J. Electrochem. Sci. Technol.* 11 (2020) 14–25, <https://doi.org/10.33961/jecst.2019.00619>.
- [70] B.P. Matadi, S. Geniès, A. Delaille, C. Chabrol, E. de Vito, M. Bardet, J.-F. Martin, L. Daniel, Y. Bultel, Irreversible capacity loss of Li-ion batteries cycled at low temperature due to an untypical layer hindering Li diffusion into graphite electrode, *J. Electrochem. Soc.* 164 (2017) A2374–A2389, <https://doi.org/10.1149/2.0491712jes>.
- [71] P. Li, H. Kim, S.T. Myung, Y.K. Sun, Diverting exploration of silicon anode into practical way: a review focused on silicon-graphite composite for lithium ion batteries, *Energy Storage Mater.* 35 (2021) 550–576, <https://doi.org/10.1016/j.ensm.2020.11.028>.
- [72] A.A. Iurchenkova, T. Kallio, E.O. Fedorovskaya, Relationships between polypyrrole synthesis conditions, its morphology and electronic structure with supercapacitor properties measured in electrolytes with different ions and pH values, *Electrochim. Acta* 391 (2021) 138892, <https://doi.org/10.1016/j.electacta.2021.138892>.
- [73] D.W. Lee, S.H. Lee, Y.N. Kim, J.M. Oh, Preparation of a high-purity ultrafine $\alpha\text{-Al}_2\text{O}_3$ powder and characterization of an Al_2O_3 -coated PE separator for lithium-ion batteries, *Powder Technol.* 320 (2017) 125–132, <https://doi.org/10.1016/j.powtec.2017.07.027>.
- [74] B. Stiaszny, J.C. Ziegler, E.E. Krauß, J.P. Schmidt, E. Ivers-Tiffée, Electrochemical characterization and post-mortem analysis of aged $\text{LiMn}_2\text{O}_4\text{-Li(Ni}_0.5\text{Mn}_0.3\text{Co}_0.2\text{)O}_2$ /graphite lithium ion batteries. Part I: cycle aging, *J. Power Sources* 251 (2014) 439–450, <https://doi.org/10.1016/j.jpowsour.2013.11.080>.
- [75] R. Fu, S.Y. Choe, V. Agubra, J. Fergus, Modeling of degradation effects considering side reactions for a pouch type Li-ion polymer battery with carbon anode, *J. Power Sources* 261 (2014) 120–135, <https://doi.org/10.1016/j.jpowsour.2014.03.045>.
- [76] J. Park, S.S. Park, Y.S. Won, In situ XRD study of the structural changes of graphite anodes mixed with SiO_x during lithium insertion and extraction in lithium ion batteries, *Electrochim. Acta* 107 (2013) 467–472, <https://doi.org/10.1016/j.electacta.2013.06.059>.
- [77] Z.Q. Li, C.J. Lu, Z.P. Xia, Y. Zhou, Z. Luo, X-ray diffraction patterns of graphite and turbostratic carbon, *Carbon N. Y.* 45 (2007) 1686–1695, <https://doi.org/10.1016/j.carbon.2007.03.038>.
- [78] J. Guo, Y. Li, J. Meng, K. Pedersen, L. Gurevich, D.I. Stroe, Understanding the mechanism of capacity increase during early cycling of commercial NMC/graphite lithium-ion batteries, *J. Energy Chem.* 74 (2022) 34–44, <https://doi.org/10.1016/j.jechem.2022.07.005>.
- [79] Q. Liu, S. Li, S. Wang, X. Zhang, S. Zhou, Y. Bai, J. Zheng, X. Lu, Kinetically determined phase transition from stage II (LiC_{12}) to stage I (LiC_6) in a graphite anode for Li-ion batteries, *J. Phys. Chem. Lett.* 9 (2018) 5567–5573, <https://doi.org/10.1021/acs.jpcclett.8b02750>.
- [80] M. Shimizu, H. Usui, T. Suzumura, H. Sakaguchi, Analysis of the deterioration mechanism of Si electrode as a Li-ion battery anode using Raman microspectroscopy, *J. Phys. Chem. C* 119 (2015) 2975–2982, <https://doi.org/10.1021/jp5121965>.
- [81] D. Ma, Z. Cao, A. Hu, Si-based anode materials for li-ion batteries: a mini review, *Nano-Micro Lett.* 6 (2014) 347–358, <https://doi.org/10.1007/s40820-014-0008-2>.